2019

Intrapulmonary Inoculation of Multicellular Tumor Spheroids to Construct an Orthotopic Lung Cancer Xenograft Model that Mimics Four Clinical Stages of Non-small Cell Lung Cancer

Yingbo Huang
University of the Pacific, y_huang10@u.pacific.edu

INTRAPULMONARY INOCULATION OF MULTICELLULAR TUMOR SPHEROIDS TO CONSTRUCT AN ORTHOTOPIC LUNG CANCER XENOGRAFT MODEL THAT MIMICS FOUR CLINICAL STAGES OF NON-SMALL CELL LUNG CANCER

by

Yingbo Huang

A Thesis Submitted to the

Graduate School

In Partial Fulfillment of the

Requirements for the Degree of

MASTER OF SCIENCE

Thomas J. Long School of Pharmacy and Health Sciences
Drug Delivery and Targeting

University of the Pacific
Stockton, California

2019

INTRAPULMONARY INOCULATION OF MULTICELLULAR TUMOR SPHEROIDS TO CONSTRUCT AN ORTHOTOPIC LUNG CANCER XENOGRAFT MODEL THAT MIMICS FOUR CLINICAL STAGES OF NON-SMALL CELL LUNG CANCER

By

Yingbo Huang

APPROVED BY:

Thesis Advisor: Xin Guo, Ph.D.

Committee Member: Melanie Felmlee, Ph.D.

Committee Member: Jesika S. Faridi, Ph.D.

Department Chair: William K. Chan, Pharm.D., Ph.D.

Dean of Graduate School: Thomas Naehr, Ph.D.

ACKNOWLEDGEMENTS

The work presented here would not have been possible without the help of many people. I would first and foremost like to thank my advisor Dr.Xin Guo. I had the distinct pleasure of working with him. As an experienced mentor with a critical mind and deep-seated enthusiasm, Dr.Guo provides insightful guidance and incessant support when I was struggling with the endless experiments. His principles, efforts and encouragement motivate me for being an independent and well-rounded researcher.

I would also like to thanks my thesis committee members Dr.Melanie Felmlee and Dr. Jesika S. Faridi for their valuable contribution to my thesis. They were an excellent source of advice, ideas and support. I also like to acknowledge Dr.Xiaoling Li, for introducing the program between University of the Pacific and China Pharmaceutical University. I also like to thanks Dr. William K. Chan, Dr.Roshanak Rahimian and Dr.John C. Livesey for providing resources to support my research.

I would like to thank Guo's group member both past and present. I especially want to thank Yifan Lu who has given me not only assistance on my project and life as a graduate student but also his advice in developing my career. I cannot thank Yifan enough for the help he provided. I also want to thank Mallika Vadlamudi, who is always supportive to me and provided efforts in this project. The uncountable discussions with her are critical for the work I presented here. I would like to thanks Dr.Shen Zhao, Xinyu Pei, Ruiqi Huang, Weizhou Yue, Zhongyue Yuan and Zizhao Xu for their help in Guo's group. It is my pleasure of working with them over the years.

My friends have been my anchor through these years. I want to thank Zhixin, Dengpan, Hao, Xingchen and Chao for their friendship, encouragement, good times, and crazy as needed. A special thanks to Chao who spent times and efforts to help me further understand this industry. Thanks, Jinyun, Jieyun, Yujie, Michael, Razan for their help in training me many techniques.

Finally, I would like to thank my family. Their unconditional love supports, prepares and strengths me to walk through this tough but invaluable journey.

Intrapulmonary Inoculation of Multicellular Tumor Spheroids to Construct an Orthotopic Lung Cancer Xenograft Model that Mimics Four Clinical Stages of Non-small Cell Lung Cancer

Abstract

By Yingbo Huang

University of the Pacific
2019

Lung cancer leads in mortality among all types of cancer in the US and Non-small cell lung cancer (NSCLC) is the major type of lung cancer. Immuno-compromised mice bearing xenografts of human lung cancer cells represent the most common animal models for studying lung cancer biology and for evaluating potential anticancer agents. However, orthotopic lung cancer models based on intrapulmonary injection of suspended cancer cells feature premature leakage of the cancer cells to both sides of the lung within five days, which generates a quick artifact of metastasis and thus belies the development and progression of lung cancer as seen in the clinic.

Based on intrapulmonary inoculation of multicellular spheroids (MCS), we have developed the first orthotopic xenograft model of lung cancer that simulates all four clinical stages of NSCLC progression in mice over one month: Stage 1 localized tumor at the inoculation site; Stage 2 multiple tumor nodules or larger tumor nodule on the same side of the lung; Stage 3 cancer growth on heart surface; and Stage 4 metastatic cancer on both sides of the lung. The cancer development was monitored conveniently by in vivo fluorescent imaging and validated by open-chest anatomy, ex vivo fluorescent imaging, and histological studies. The model enjoys

high rates of postoperative survival (100%) and parenchymal tumor establishment (88.9%). The roughness of the inoculated MCS is associated negatively with the time needed to develop metastatic cancer ($p=0.0299$).

In addition, we have constructed a co-culture MCS that consisted of A549-iRFP lung cancer cells and WI38 normal human fibroblast cells. The pro-proliferation effect and the high expression of α-smooth muscle actin (α-SMA) by the co-cultured WI38 cells indicated their transformation from normal fibroblasts to cancer-associated fibroblasts (CAFs). The morphology of the co-culture MCS features a round shape, a tight internal structure, and quicker development of roughness. The large roughness value of co-culture MCS suggests that small co-culture MCS could be inoculated into mice lung with a small needle to reduce the surgical trauma.

Taken together, a new orthotopic model of NSCLC has been developed, which would facilitate future development of medications against lung cancer.

TABLE OF CONTENTS

LIST OF TABLES

Table

LIST OF FIGURES

Figure

LIST OF ABBREVIATIONS

NSCLC	Non-small cell lung cancer
SCLC	Small cell lung cancer
PD-L1	Programmed death ligand-1
EGFR	Epidermal growth factor receptor
ALK	Anaplastic lymphoma kinase
TME	Tumor microenvironment
CAFs	Cancer-associated fibroblasts
ECM	Extracellular matrix
LKB1	Liver kinase B1
IL6	Interleukin-6
STAT3	Signal transducer and activator of transcription 3
CDX	Cell-line derived xenograft
PDX	Patient-derived xenograft
GEMM	Genetically engineered mouse model
CT/PET	Computed tomography-positron emission tomography
MRI	Magnetic resonance imaging
GFP	Green fluorescence protein

RFP	Red fluorescence protein
APC	Adenomatous polyposis coli
Rb1	Retinoblastoma protein
TSG	Tumor suppressor gene
VEGF	Vascular endothelial growth factor
OS	Overall survival
NIR	Near-infrared
iRFP	Near-infrared fluorescent protein
MCS	Multicellular tumor spheroid
H&E	Hematoxylin and eosin
TNF	Tumor necrosis factor
TGF-β	Transforming growth factor beta
HGF	Hepatocyte growth factor
SDF1	Stromal cell-derived factor 1
EMT	Epithelial-to-mesenchymal transition
α-SMA	α-Smooth Muscle Actin

Chapter 1: Introduction

1.1. Lung Cancer

In 2019, there are 228,150 estimated new cases and 142,670 estimated deaths from lung cancer in the US. Among all oncological diseases, lung cancer claims the highest mortality (23.5%) in the US and the most new cases in developing countries [1]. Based on histological features, lung cancer is classified either as non-small cell lung cancer (NSCLC), which is the most prevalent type (85%), or small cell lung cancer (SCLC) [2]. Tobacco smoking is the main etiology for lung cancer in countries where smoking is common. Small-Cell lung cancer (SCLC) is more common in smokers compared with never-smokers, and is characterized as highly aggressive, poorly prognosed and widely metastatic [3, 4]. The 5-year survival rate of SCLC is only 7%, much lower than NSCLC (23%) [5].

In NSCLC, lung adenocarcinoma, squamous cell carcinoma and large cell carcinoma are the common subtypes. Lung adenocarcinoma carries the histological features of acinar papilla and solid adenocarcinoma with mucin, and accounts for 40% of NSCLC. Lung adenocarcinoma tends to develop as a solid tumor in smaller airways, such as bronchioles and is usually located more along the outer edges of the lungs. About 25% of lung cancers are squamous cell carcinomas, which carries a squamous morphology and tends to be found in the central lung near the bronchi and tracheal [6]. In the clinic, NSCLC is categorized into 4 stages according to its progression: Stage 1 primary tumor localized in one side of the lung; Stage 2 multiple tumors within one side of the lung or a single tumor larger than 5 cm in diameter; Stage 3 cancer that has spread into the lymph nodes, heart surface and/or chest wall; and Stage 4 cancer that has metastasized to both sides of the lung, the fluid in the chest and/or other organs [5].

The treatment of NSCLC includes surgery, radiotherapy, first-line cytotoxic therapy (platinum drugs), targeted therapy (based on the patient's genetic alterations), and immunotherapy. According to the pathological features, patients diagnosed with squamous cell carcinoma will be given platinum-based chemotherapy or pembrolizumab when PD-L1 is largely expressed (>50% in cancer cells). For patients diagnosed with lung adenocarcinoma, the treatment varies in targeted chemotherapy, such as erlotinib (EGFR mutation) and crizotinib (ALK mutation), and immunotherapy [7]. According to the clinical stage, patients diagnosed with Stage 1 or 2 will be suggested with surgery to remove the tumor followed by adjunct therapy. For the clinical Stage 3, patients will be given chemo and radiotherapy. For patients with advanced lung cancer, chemotherapy, targeting-therapy, and immunotherapy will be given based on the molecular pathology of the tumor [5]. Therefore, the diagnosis of histological subtypes and the four stages of NSCLC progression are critical for designing the treatment.

In recent years, the critical role of the tumor microenvironment (TME) in tumorigenesis, angiogenesis and metastasis has been established. In the TME of human lung adenocarcinoma, the heterogeneity of many components such as cancer-associated fibroblasts (CAFs), vasculature system, extracellular matrix (ECM) and tumor-infiltrating immune cells are associated with poor prognosis [8].

In a solid tumor, collagens, proteoglycans, and fibronectin mainly constitute the ECM. These proteins not only build up a dense barrier to limit drug penetration, but also mediate the interactions between cancer cells and stromal cells to promote carcinogenesis. In LKB1 (tumor suppressor gene) deficient mice, collagen deposition and ECM remodeling contribute to a pathological transformation from human lung adenocarcinoma to squamous cell carcinoma [9].

CAFs have been studied in many types of cancer, including NSCLC, where the pro-tumor effects of CAFs have been shown in cancer proliferation, invasion and metastasis. Although the origin of CAFs is still unknown, the cancer cells have been known to re-educate normal fibroblasts to CAFs. For example, after being co-cultured with human lung cancer cells, the normal human fibroblast WI38 cells assumed the ability to promote cancer cell invasion [10]. CAFs, after being isolated from human lung cancer specimen, also facilitated cancer metastasis by secreting interleukin-6 (IL6) to activate the STAT3 cell signaling pathway [8, 11]. In a clinical study, the higher level of podoplanin-positive CAFs was significantly associated with higher 5-year recurrence rate in patients of Stage 1 lung adenocarcinoma [12]. Taken together, CAFs play an important role in the TME of NSCLC to stimulate the cancer growth.

Despite the basic research on NSCLC and the advances in therapeutic standards in the clinic, no general platform which reflects the features of tumor progression has been adopted for screening drug candidates. The currently available models in pre-clinical research serve specific needs, such as high-throughput drug screening or studies on tumorigenesis mechanisms. Among them, mouse models are designed to mimic the complex human cancer biology and are widely used in drug development. Mouse model in oncology research will be briefly reviewed in the next section.

1.2 Mouse Cancer Models in Pre-clinical Research

Mouse models play an essential role in pre-clinical oncology research. Whether to evaluate drug efficacy or to study the pathological mechanisms of cancer, mouse models serve to eventually benefit clinical outcomes. Mouse models are being continually optimized since the first allografts mouse model was developed in the 1960's, which helped discover the anticancer agent vincristine [13]. To date, there are four different categories of mouse models in oncology

research, namely the cell-line derived xenografts (CDX), patient-derived xenografts (PDX), environmentally induced mouse models, and genetically engineered mouse models (GEMM).

1.2.1 Cell-derived xenograft (CDX). CDX were developed in the 1980s when researchers transplanted human tumor cells into immunodeficient mice [14]. CDX quickly replaced allograft mouse models as the tool for evaluating drug candidates. The development of the NCI60 panel provides a valuable resource for CDX and further facilitated its application [15]. The predominant CDX is a subcutaneous xenograft, where the tumor develops under the skin. This tractable model has advantages such as low-cost, easy techniques, and high reproducibility. The potential of cancer metastasis in CDX is dependent on both the intrinsic characteristics of the tumor cells and their environment in the host, which can differ between tissues and organs [16]. Indeed, the anatomical site where the human cancer cells are injected influences cancer progression. The microenvironment surrounding the subcutaneous tumors does not meet the conditions for metastasis [17], whereas orthotopic implantation can better mimic the disease microenvironment. In orthotopic xenografts, cancer cells are injected into the organ of its origin to study the metastasis pattern. The cancer growth in an orthotopic xenograft features local tissue invasion. Moreover, subcutaneous xenografts possess unfaithful vasculature that limits cancer metastasis, which in turn limits the model's ability to predict drug response in the clinic [18]. For example, hydralazine was shown to enhance the effect of reducing blood flow in a subcutaneous xenograft. However, the effect later was shown to be ineffective as a therapeutic strategy to inhibit the blood flow both in the clinic and an orthotopic rodent model [19].

Compared to subcutaneous xenografts, the main disadvantages of orthotopic xenograft models are the complex surgical procedures and the difficulty in tracking tumor growth. The

technical difficulties vary by an disease. Injection of human breast cancer cells into the mammalian fat pad to build orthotopic breast cancer model is readily achievable in most laboratories that carry out animal studies [20]. However, the construction of orthotopic lung cancer and glioblastoma models need well-trained operators and specialized equipment [21]. Many clinically used imaging methods such as small animal CT/PET, MRI, ultrasound, x-ray can also be used to monitor tumor growth on mice. However, these methods require expensive instruments, a relatively long-time for each scan, and some also involve unhealthy radiation [22]. In order to trace the cancer progression, invasion and metastasis efficiently in orthotopic xenografts, researchers have developed "labeled" tumor cell lines. These cells carry proteins which could be illuminated, such as green fluorescence protein (GFP), red fluorescence protein (RFP), or firefly luciferase. These proteins are activated either by fluorescent light or an enzymatic reaction to locate the cancer cells by their emission light. The advantages of labeled tumor cells are that the progress/response of the tumor can be tracked with efficient imaging, the internal tumors can be measured, and cancer metastasis can be monitored [23].

1.2.2 Patient-derived xenograft (PDX). As a useful tool for personalized medicine, patient-derived xenograft (PDX) models can faithfully recapture the histological and genetic features of a particular patient's cancer. Typically, PDX are constructed in mice by subcutaneously inoculating a fresh tumor graft that is surgically derived from a patient [24]. This model is better aligned with the disease condition compared to CDX. PDX in mice can maintain the same molecular and pathological characteristics of a patient's cancer over limited passage expansion. Moreover, the remaining stromal cells in the tumor graft can be retained over several passages, providing an accurate tumor microenvironment [25]. By selectively

implanting the tumor grafts, PDX is currently the only model that could reflect the hypermutant tumor progression and the intra-tumor heterogeneity [26].

PDX show great potential in precisely predicting drug response. A high-throughput screening study to predict drug response by employing the PDX model shows reproducibility and clinical translatability. Almost 1000 PDX models across six types of cancer have been developed, their genotype and drug response analyzed, and their corresponding clinical outcomes correlated [27].

Despite PDX's encouraging advances, its's application is limited by the high cost and the large variations in tumor growth. The lack of collaboration between clinics and research labs prohibits most research labs from utilizing PDX to evaluate therapeutic agents. Moreover, the engraftment rate of PDX varies by tumor types, level of gene mutations, and molecular complexity. Another limitation of PDX is that the inoculation site of the patient-derived graft is mainly subcutaneous. The technical challenges in the grafting and the following imaging have so far restricted the studies on PDX in academia [15, 25, 28].

1.2.3 Environmentally induced mouse model. The environmentally induced mouse models have two main applications in testing potential carcinogens for human and in studying the causes of cancer. Such models started with coal tar to induce skin cancer 100 years ago and have now included many environmental carcinogens, such as chemicals, radiation and pathogens [29]. Animal models of a variety of cancers, including skin [30], lung [31], liver [32] and colon cancer [33], have been established in this manner. These models closely mimic the genetic and molecular heterogeneity of the corresponding human cancer. A comparison of gene variations between urethane-induced lung cancer mouse model and human lung adenocarcinoma revealed an overlap of the oncogene mutations. Many of the frequently mutated genes in human lung

cancer, such as Arid1b, ALK, APC, JAK2, Mll2, Rb1, were also mutated in environmentally induced mouse tumors [31].

However, the environmentally induced mouse models are criticized for their long latent-period and large variations in tumor growth. A relatively large animal number is needed for the study design [25]. Therefore, the application of this type of model remains limited in current cancer research.

1.2.4 Genetically engineered mouse model (GEMM). Transgenic mice were first generated in the 1980s by injecting the recombinant oncogenes MK into mouse eggs [25]. Subsequently, tumor suppressor gene (p53) knockout mice were developed in 1992 [34]. However, in the oncomice or tumor suppressor gene (TSG) knockout mice, the genetic mutations exist in all cells of the animal. This wide expression of transgenes causes early death of the transgenic mice and thus prohibits the normal progress of cancer [35]. To address these problems, more complex mouse models that carry mechanisms of TSG inactivation or oncogene activation have been developed. Such conditional GEMM can induce gene mutations at a specific tissue based on a site-specific recombinase system, such as *Cre-loxP*, *Cre-ERT*, *Flp-FRT*, and *Tet-on/off*. Intratracheal or intranasal administration of adenovirus can deliver *Cre* recombinase that activates *Kras* to build a non-small cell lung cancer model. The tumor formation and progression starts 2–3 weeks after administration, and the median survival rate was around 150 days. The cancer was initiated at multiple places and progressed sequentially according to a four-stage grading system. Another more aggressive model of NSCLC was created by combining the knockout of the tumor suppressor gene *p53* with the activation of the oncogene *Kras* [36]. For another example, a dual-recombinase system that combined *Cre-loxP* and *Flp-FRT* allowed a multistep genetic manipulation in mice. This sequential induction of

gene mutations mimicked the increase of mutation burden during the progression of pancreatic cancer [37]. Overall, GEMM represent valuable tools in studying cancer initiation and progression.

GEMM have made reliable predictions in evaluating targeted anticancer therapy. Compared to first-line chemotherapy alone, combining the chemotherapy with an anti-vascular endothelial growth factor (VEGF) antibody, Bevacizumab increased the median overall survival (OS) in NSCLC patients by 2 months. In a corresponding study on a *Kras* mutated GEMM model of NSCLC, the combination showed a similar improvement (2.5 months) of OS, thus demonstrating that GEMM could retrospectively reproduce patients' response to an oncological treatment in clinic [38].

Despite many advantages of GEMM both in drug development and in basic oncological research, several drawbacks limit its application. First, early deaths from the burden of multiple primary tumors per animal in GEMMs hamper their simulation of cancer metastasis. Secondly, one or two genetic variations dominate in GEMM, resulting in less tumor heterogeneity. Third, GEMM is time-consuming and expensive, which limit its application in many labs [25, 35].

1.2.5 Status quo and future challenges. A statistical study on a total of 949 oncology publications found that 65% of them utilized mouse models. CDX was used in 82%, GEMM in 24%, PDX in 7%, and environmentally induced mouse model in 6% of these publications (Fig.1) [25]. 109 studies used more than one type of the mouse models, the percentages added up to more than 100%. Overall, the CDX was by far the most widely used animal models in pre-clinical research.

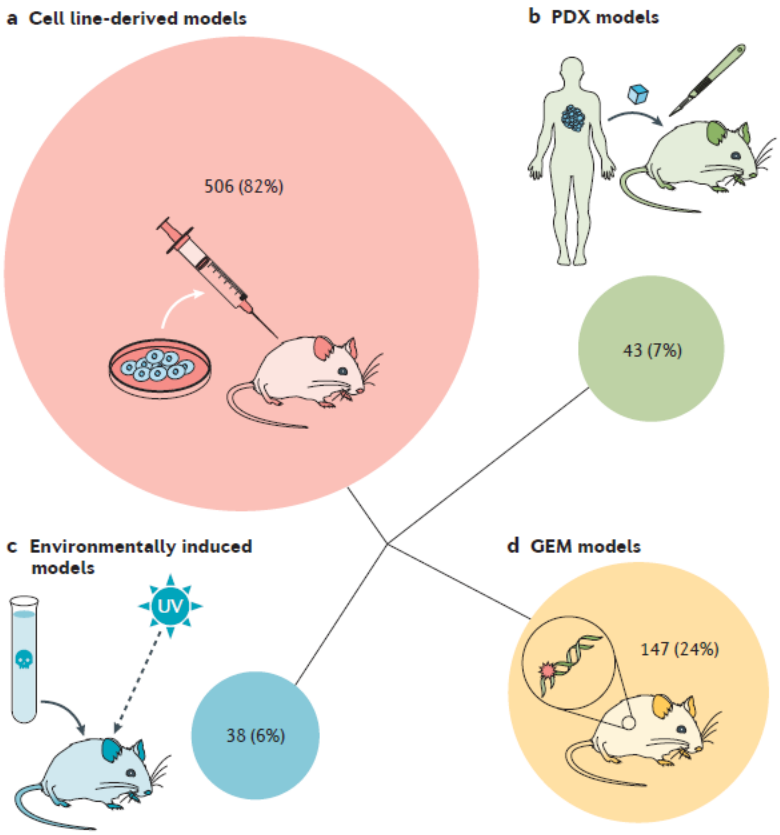

Figure 1: Percentage of usage by different types of tumor models in pre-clinical studies that were published in 2016 [25]

Different mouse models are used at different frequencies for different types of cancers. The CDX model is used predominantly in melanoma (95%), breast cancer (93%) and brain cancer (91%). On the other hand, 60% of pancreatic cancer models are GEMM. This is probably because of the successful identification of the genes that can enhance the development of pancreatic cancer in GEMM. Environmentally induced model is used in liver cancer and colon cancer because of the easy administration of the carcinogens into the digestive system [25]. (Fig.2)

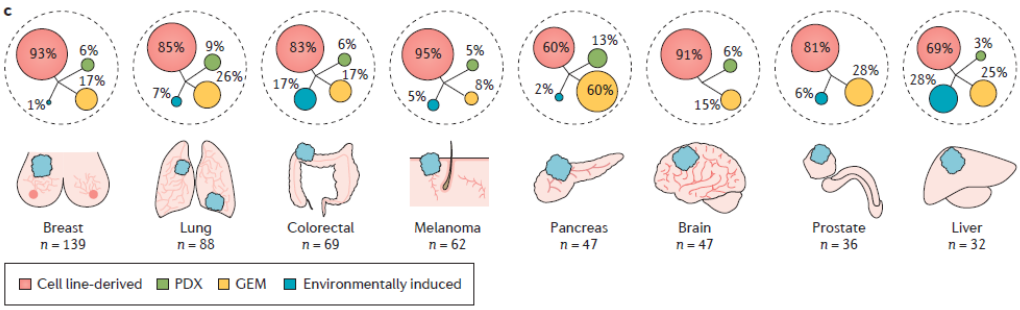

Figure 2: Frequency distribution of cancer models for eight common solid tumor types. [25]

One of the major concerns of mouse tumor models is the precise reflection of cancer progression. In general, cancer initiates with neoplastic cells, then grows into a small tumor nodule, then invades the surrounding tissue and develops its vasculature, and eventually metastasizes. The de novo growth of tumors in GEMM and environmentally induced mouse model reflects tumorigenesis, but the primary tumors are multi-focal, which leads to early organ failure and substantially shortens the lifespan of the mice. Thus, these two models primarily mimic cancer metastasis [39]. As to the PDX and CDX models, the subcutaneous implantation of tumors leads to a non-autochthonous growth of cancer. The site of engraftment significantly influences the metastasis potential of the tumor, and for many types of cancer cells, the subcutaneous xenografts in mice rarely progress to metastasis. In contrast, orthotopic transplantation models are supported by a relevant tumor microenvironment and tend to well reflect cancer metastasis [40]; however, the CDX model is mainly limited by its unreliable prediction of targeted therapy [15].

The main challenges of constructing a reliable pre-clinical mouse cancer model to benefit drug development are: (1) development of a single focal primary tumor; (2) recapitulation of

cancer progression and metastasis; (3) convenient imaging to track the cancer growth; and (4) high efficiency and low cost that would facilitate usage for laboratory research.

1.3 CDX Model of NSCLC

The establishment of the NCI60 panel has facilitated the development of CDX models. Around 200 cell lines for NSCLC have been reported in biomedical research. Allograft models that were constructed from murine lung cancer cells showed aggressive growth and distant metastasis. Mice that were subcutaneously injected with Lewis lung carcinoma cells showed multiple tumor nodules in the lung [41]. However, the molecular and pathological differences between the human cancer cells and murine cancer cells mislead the assessment of efficacy of drug candidates. Hence, xenograft models using human cancer cells were developed in the 1990s [25]. For NSCLC, there are four methods of constructing a CDX model that will be introduced as below.

First, human cancer cells or grafts can be inoculated subcutaneously into immunodeficient mice. Due to its easy technique (no anesthesia, easy injection) and convenient tumor measurement, 58% of the CDX models in literatures were based on subcutaneous engraftment [25]. In NSCLC, hypoxia and angiogenesis both play a major role in solid tumor progression; however, in subcutaneous xenografts, cancer progresses differently because of the irrelevant host microenvironment. CDX models from subcutaneous injection of A549 cells showed strong hypoxia conditions compared with either the orthotopic implantation models or the spontaneous genetic models. Interestingly, the average oxygen levels of lung tumors are higher than those of other solid tumors in patients, which would yield a less hypoxic condition in the clinic than the subcutaneous models reflect [42].

To address this shortcoming, orthotopic lung cancer models have been developed either by surgical implantation of tumor grafts, or by direct injection of suspended cancer cells into the lung [43]. Surgical implantation utilizes tumor fragments from fresh tumors or subcutaneously-grown tumors of NSCLC cells. One tumor graft was inserted into the lung parenchyma of each mouse through the open chest surgery. The tumor graft can be inoculated at the desired site to mimic the tumor initiation and the histological analysis showed a confined tumor nodule in the lung. Despite the advantages of the surgical implantation method, the technical difficulties, specialized facilities (ventilator) limit the application of this model [44].

Transpleural injection of cancer cell suspensions is another method to build orthotopic lung cancer xenografts. A small incision on the skin is cut on the back side of the mice, after separation of the muscle and fat, the cancer cell suspension is injected into the lung parenchyma through the intercostal space [45, 46]. This approach avoids the complicated thoracotomy and special requirement of equipment. Moreover, this method has a significantly lower postoperative mortality rate (3%) than the surgical transplantation (60%), and therefore requires fewer mice to finish the study [43].

One problem with pleural seeding [43] is that when the needle penetrates the pleural cavity, it is unknown whether the needle is inserted into the lung parenchyma. Therefore, the location where the cell suspension was injected is either in the lung parenchyma or in the thoracic cavity. Furthermore, because of the fluidity of the suspension and the respirational movements of the lung tissue, the cancer cells tend to prematurely leak from the injection site to both sides of the lung within five days. Such leakage generates a quick artifact of metastasis and thus belies the development and progression of lung cancer as seen in the clinic [43, 45, 47, 48]. To overcome this problem, a very small volume of cell suspension has been injected by the same

method. 500 Lewis lung carcinoma cells were suspended in 2 µl volume PBS, and the cell suspension was injected into the left lung of mice. The open chest anatomy showed a confined localized tumor nodule on the left lung. The same experiment was performed using A549, a human lung adenocarcinoma cell, at a seeding density of 10^4 cells suspended in 1µl volume. The tumor nodule can be observed in 6 weeks after injection, and no distant metastasis has been found [49]. The model mimics an early stage of NSCLC and can be utilized to study cancer progression. However, because of the small volume, the cells require multiple times of concentration in preparing the suspension. Furthermore, the xenograft establishment needs a relatively longer time, which limits the model's efficiency for drug discovery in industry.

Injection of suspended cancer cells into the blood circulation can quickly generate mice carrying cancer metastasis. Intracardiac injection of A549 cell suspension into mice showed a significant high potential of cancer metastasis [50]. Although such an experimental model offers an efficient way to study cancer metastasis, it belies the primary tumor initiation and therefore fails to reflect the typical cancer metastasis in the clinic [51].

In summary, there are four approaches to construct the CDX model of NSCLC. Despite the convenience in building a subcutaneous xenograft, its lack of clinical relevance turns us to studying the orthotopic xenograft model. Further, we need to find an imaging method to track the cancer progression in an orthotopic lung cancer model. There are several imaging methods to monitor cancer growth in small animals, such as CT/PET, bioluminescence, fluorescence, MRI, ultrasound, and X-Ray. Some of these methods will be introduced below.

1.4 Fluorescent Protein in Small Animal Imaging

A noninvasive *in vivo* imaging method can greatly enhance oncology research. The size and location of tumors can be shown precisely by radiation imaging systems such as a small animal PET imaging system, which provides a three-dimensional measurement of tumors in live animals [52]. However, the use of radioactive contrast agents could endanger the animal health, along with other ethical issues.

As an alternative, optical imaging is much safer and highly versatile. Green fluorescent protein (GFP) lighted up the oncological research in the laboratory in visualizing and understanding cancer progression. The inventor of GFP was awarded the Nobel Prize in chemistry in 2008 [53]. Whereas the fluorescent signal of GFP is typically used for intravital microscopy, deep tissue imaging of live animal (>500 μm) requires the use of near-infrared light (NIR) [54]. Compared to other light signals, NIR (650 nm to 900 nm in wave length) is absorbed less by hemoglobin and water, [55] and enjoys low body autofluorescence, making it an excellent choice for small animal imaging [56]. The development of GFP-like fluorescent proteins, which have NIR fluorescence, promotes research in studying metastatic cancer by whole-body imaging in real time.

An NIR fluorescent protein (iRFP) was developed in 2011 from bacterial phytochrome photoreceptors, with an excitation wavelength at 690 nm and emission wavelength at 713 nm. The iRFP carries high stability and low cytotoxicity, and provides a strong fluorescent signal that can penetrate as deep as 18.1 mm in mice. iRFP later have been utilized in many research fields to broaden the applications of noninvasive imaging *in vivo* [56].

1.5 Three-dimensional Multicellular Tumor Spheroids (MCS)

Recently, three-dimensional multicellular spheroids (MCS) have emerged as an attractive *in vitro* model of cancer. Compared to cancer cell monolayers, MCS better mimic the microenvironment inside solid tumors [57, 58]. The monolayer cells are inadequate in reflecting the unique solid structure and tumor microenvironment, such as cell-cell interaction, which are essential for the functions of tumors. In contrast, MCS of sufficient size assumes a hypoxic and necrotic core similar to that in solid tumors *in vivo*, which also plays a key role in solid tumors' resistance against anticancer drugs [58].

In pre-clinical research, MCS have been developed to bridge between conventional 2D cell models and *in vivo* tumor models. Further, MCS have been inoculated into mice to construct orthotopic models of breast cancer and prostate cancer [59, 60]. Patient-derived MCS have been transplanted into mice to construct PDX model of prostate cancer. The PDX showed metastasis and osteosclerosis when tumor spheroids were implanted orthotopically [59]. However, no literature has been found to date on the construction of orthotopic animal models of lung cancer using MCS.

1.6 Statement of Problems and Hypothesis

The traditional NSCLC xenografts based on inoculation of human lung cancer cells in suspension feature premature leakage of cancer cells from the injection site, which generates a quick artifact of metastasis and thus belies the development and progression of lung cancer as seen in the clinic. Such a model does not simulate the clinical stages of NSCLC, and therefore may misguide the pre-clinical discovery of potential drugs against lung cancer. In contrast, 3D MCS carries a tight solid texture, which could minimize the premature leakage of cancer cells from the injection site after being inoculated into the lung. Moreover, MCS better mimic the TME, which would allow its orthotopic xenograft to better establish and progress *in vivo*.

Intrapulmonary inoculation of MCS would also allow the development of only one primary tumor per lung. Taken together, we hypothesize that MCS of human cancer cells can be inoculated orthotopically into mice to construct a xenograft model that better simulates NSCLC in the clinic than orthotopic injection of cancer cells in suspension.

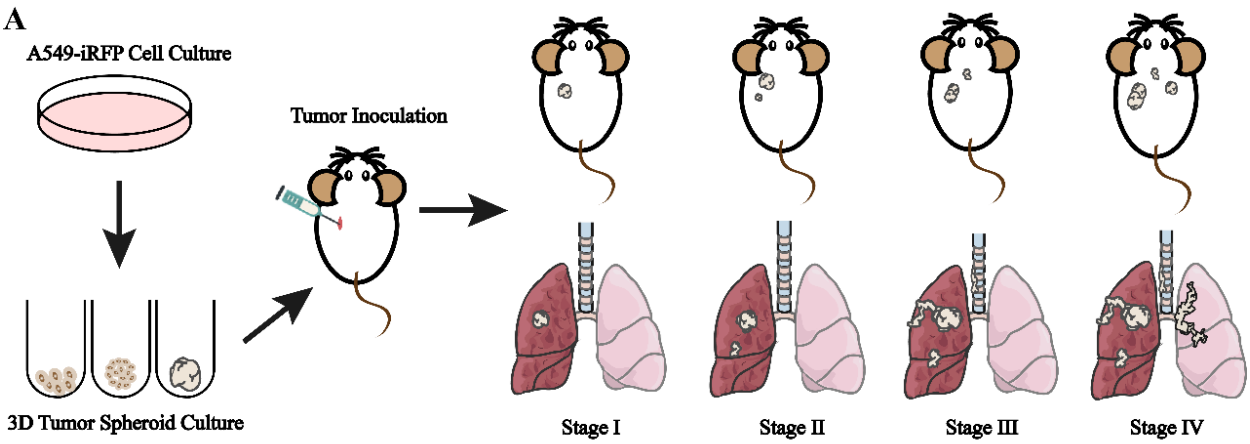

Figure 3: Schematic illustration of study design

Chapter 2: *In Vitro* Characterization of Multicellular Tumor Spheroids (MCS) Using A549-iRFP Cell

2.1 Introduction

In pre-clinical research, anticancer drug candidates need to be evaluated for efficacy, toxicity, and safety before being considered for clinical trial. The *in vitro* screening of therapeutic agents is the first step in this process. Typically, 2D monolayer cell culture has been used as a platform for testing of treatments, but the data from such platforms often poorly predict outcome of the following clinical studies [61]. The following are some major reasons for such poor predictions. First, a 2D cell culture lacks certain features of a solid tumor that causes their resistance against anticancer agents [62], which allows many ineffective agents to be passed on for further *in vivo* studies. For example, the lack of appropriate physiological barriers in monolayer cell culture limit its prediction of intratumoral drug penetration. Secondly, the lack of cell-cell interaction, and somatic cells in the traditional 2D cell culture reflects an incomplete tumor microenvironment. Therefore, an *in vitro* model that can capture more physiological features of solid tumors than the conventional 2-D culture is needed for pre-clinical studies to better predict drug effects in the clinic.

In 1971 Sutherland et al. first introduced tumor spheroids as a model for nodular carcinoma research [63]. Since then, various multicellular tumor spheroids (MCS) such as scaffolds, scaffold-free MCS, and microfluidics provide new models for screening therapeutic agents [58]. Many unique characteristics of MCS have been discovered, including cellular heterogeneity and interactions, 3D architecture, internal metabolic heterogeneity, extracellular matrix deposition, hypoxia and the presence of cancer stem cells [62]. All these characteristics

have been found in clinical studies of solid tumors. Taking these advantages into consideration, 3D MCS not only mimic the physiological features of a solid tumor but also serve as better models to predict the clinical behavior of anticancer agents.

Although spheroids are often used to mimic the *in vivo* environment of the solid tumor, they can also be inoculated into the animal in order to study angiogenesis and tumor/stroma interaction. Recently, human glioblastoma spheroids have been implanted into immunodeficient rats to study cancer invasion and tumoral vasculature formation [64]. The development of patient derived xenograft (PDX) models benefit personalized medicine. However, the limited tumor tissues from patients hinder the application of PDX model in pre-clinical studies [25]. Construction of MCS from patients' tumor tissue followed by their inoculation into animals can further expand the utilization of PDX models. Researchers at Stanford University have transplanted 136 patient-derived prostate cancer MCS into mouse to promote personalized treatment [59]. However, no literature has been found to date on the construction of orthotopic animal models of lung cancer using MCS. The construction and characterization of A549-iRFP MCS are reported in this Chapter in order to later inoculate such MCS into mice lung. The spheroid can form a tight and round shape with 15 days growth. The fluorescent signal shows a strong linear correlation with the spheroid viability and volume. The MCS also presents with a necrotic core.

2.2. Materials and Methods

2.2.1. Cell line and reagents. Human lung adenocarcinoma A549-iRFP (λ_{ex} =690 nm, λ_{em} = 713 nm) was purchased from Imanis Life Sciences (Rochester, MN). Cell culture reagents, if not specified, were purchased from Corning Life Science. A549-iRFP was grown in DMEM cell culture media with 10% Fetal bovine serum (Gemini Bio-Products, CA), 1% penicillin-

streptomycin (Corning Life Science, US), and 1 µg/ml puromycin (Alfa Aesar, US). All cells were maintained at 37℃ and 5% CO_2. Falcon® 96-well Black/Clear Flat Bottom Microplate and 96-well Spheroid Microplate were purchased from Coring Life Science. Tumor spheroids were constructed with collagen, which was purchased from Fisher Scientific (Pittsburgh, PA). Cell viability was measured using CellTiter 96® AQueous One Solution Cell Proliferation Assay (Promega Corporation, US). The spheroid viability was measured by CellTiter-Glo® 3D Reagent (Promega Corporation, US). Invitrogen™ LIVE/DEAD™ Viability/Cytotoxicity Kit were purchased from Thermo-fisher. 4% formaldehyde in PBS for tissue fixation was purchased from Fisher Scientific. Paraplast was purchased from Sigma (St. Louis, MO) for tissue embedding. Hematoxylin and Eosin were purchased from VWR International, (Radnor, PA).

2.2.2. Fluorometric characterization of A549-iRFP monolayer cells. A549-iRFP cells were seeded onto Falcon™ 96-Well flat-bottom tissue culture microplates (Corning Life Science, US) at 0, 1000, 2000, 4000, 6000, 8000, 10000, and 12000 cells/well. The fluorescent signal (λ_{ex} =685 nm, λ_{em} = 700 nm) was monitored by an Odyssey® Infrared Imaging 205 System (LI-COR® Biosciences, Lincoln, NE, USA) at the 700 nm channel. The cell viability was measured using the CellTiter 96® AQueous One Solution Cell Proliferation Assay (Promega Corporation, US). The UV absorbance at 490 nm was recorded on a Synergy HTX microplate reader (BioTek, US).

2.2.3. Construction of MCS using A549-iRFP cell. A549-iRFP cells were seeded onto 96-well Corning spheroid microplate (Corning Life Science, US) at 4000 cells/well in 100 µl/well of the aforementioned growth medium that was supplemented with 0.3% collagen (Gibco, US). The microplate was centrifuged at 300 × g for 7 minutes on an Eppendorf Centrifuge 5810R. The cells were cultured for 48 hours and then supplemented with another 100

µl/well growth medium without collagen. Every two days thereafter, 100 µL of the growth medium in each well was replaced with 100 µl fresh growth medium without collagen.

2.2.4. *In vitro* Characterization of A549-iRFP MCS. The growth and morphology of MCS were monitored by a Keyence (US) BZ-X700 fluorescence microscope. The volume of spheroids was calculated every two days from their bright-field images using the ReVisP software from MATLAB. To calculate the roughness of an MCS, the outline of its bright-field image was traced by two concentric ovals, where the outer oval includes the edged of the MCS outline and inner oval excluded them. To calculate the roughness of an MCS, the outline of its bright-field image was carefully traced by a line (outer line, OL) to enclose the MCS image with the rough edges; the base of the rough surface was traced by another line (inner line, IL) to enclose the MCS image except for the rough edges. The roughness of MCS was calculated by the equation: Roughness (mm) = $(A_{OL}-A_{IL}) / L_{IL}$, where A_{OL} is the area enclosed by OL, A_{IL} is the area enclosed by IL, and L_{IL} is the length of IL. The fluorescence of living MCS was recorded by an Odyssey® Infrared Imaging 205 System (LI-COR® Biosciences, Lincoln, NE, US) at the 700 nm channel.

For the viability assay, each MCS was suspended in 100 µl growth medium, transferred into a well in an opaque-walled 96-well microplate, and mixed with 100 µl CellTiter-Glo® 3D Reagent (Promega Corporation, US). The microplate was covered with aluminum foil, agitated for 5 minutes, and incubated at room temperature for an additional 25 minutes. The luminescence was then recorded by a Synergy HTX microplate reader (BioTek, US).

2.2.5. Imaging of live and dead cells in A549-iRFP MCS. MCS were cultured in 96-well spheroids microplate until the diameter reached 500 µm. MCS were transferred to a glass Petri dish and incubated with a LIVE/DEAD™ Cell Imaging Kit (ThermoFisher, US) for 45

minutes at 37 °C. The spheroids were then washed 3 times with PBS and imaged on a Leica DMIRE2 confocal microscope (λ_{ex}= 491 nm, λ_{em}= 513 nm for live cells, λ_{ex}= 561 nm, λ_{em}= 607 nm for dead cells). Images were analyzed using the ImageJ software.

2.2.6. Histological analysis of A549-iRFP MCS. MCS were transferred into 6-well plates three days, six days and twenty days after seeding and washed 3 times with PBS. MCS were fixed with 4% formaldehyde at room temperature for 1 hour. After fixation, MCS were washed with PBS and dehydrated sequentially with 70%, 80%, 95%, and absolute alcohol for 1 hour each. After dehydration, MCS were incubated with Safeclear II (Xylene substitute) for 1 hour before being embedded into paraffin. MCS were then submerged into melted paraffin at 60 ºC for 1 hour. The MCS was embedded into the paraffin and quickly solidified for 10 minutes in the fridge. MCS were then cut into 10 µm-thick sections by a HM 325 Rotary Microtome and stained with H&E based on standard protocol. The histological images were then obtained on the Keyence fluorescence microscope BZ-X700 (US).

2.2.7. Standard protocol of H&E staining. Slides containing paraffin sections were first deparaffinized and rehydrated. Slides were submerged in Safeclear II for 5 mins then blotted excess Safeclear II. Slides were rehydrated sequentially with 100% ethanol (3 times), 95% ethanol, 80% ethanol, deionized water for 5 mins each. Then slides were submerged in Hematoxalin for 3 mins and follow rinsed with tap water to allow stain to develop for 3 mins. 8-12 drops of acid ethanol (1ml concentrated HCI in 400ml 70% ethanol) were quickly dipped. Slides were rinsed with tap water again for 1 min then rinsed with deionized water for 2 mins. Slides were submerged in Eosin for 40 seconds then washed with 95% ethanol for 5 mins each. Slides were submerged in absolute ethanol three times for 5 mins each follow with Safeclear II 20 mins. Slides were covered with Permount and dried overnight.

2.3. Results

2.3.1. The near-infrared fluorescent signal of A549-iRFP monolayer cells correlated with the seeding number and the cell viability. As the fluorescent signal of the A549-iRFP cells will be used to monitor the progression of their xenograft tumors *in vivo*, we elected to first test the correlation between the fluorescent signal caught by the Odyssey Infrared Imaging 205 System and the growth of A549-iRFP cells. Increasing numbers of A549-iRFP cells were seeded into wells of a black microplate and both the fluorescence and the viability (MTS assay) of each well were measured (Fig. 4A). The fluorescent signal increased as the cell density increased (R^2=0.958, Fig. 4B). Figure 4C shows a strong linear correlation between the fluorescent signal and the cell viability (R^2 = 0.9753) as long as the seeding number falls into the linear range of both assays (< 12000 cells/well).

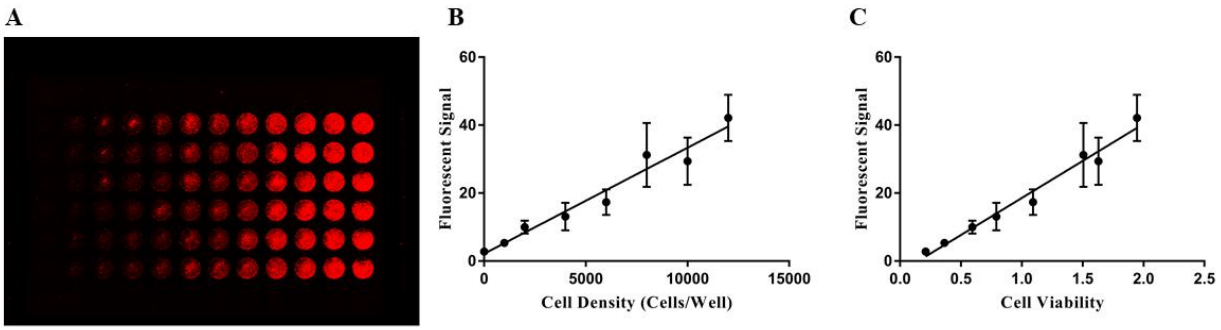

Figure 4: The fluorescent signal of monolayer A549-iRFP shows strong correlation with the cell density and cell viability. (Mean±S.D, N = 6).

2.3.2. A549-iRFP cells formed tight round-shaped tumor spheroids in the presence of collagen. A549-iRFP cells were elected to construct the MCS as lung cancer xenografts

because they were derived from the commonly used NSCLC cell line A549 and express a near infrared fluorescent protein for convenient imaging of the subsequent cancer progression *in vivo*. In order to promote the cell-cell adhesion that is needed for MCS formation, the A549-iRFP cells were seeded with 0.3% collagen in the growth medium and with centrifugation at 300 × g. The resultant A549-iRFP MCS showed a round shape, tight structure and smooth surface in the first 15 days (Fig. 5A). The volume and 3D re-construction of MCS was measured using Revisp computational modeling software. The increasing volume showed a linear relationship with time (R^2=0.9622, Fig. 5B).

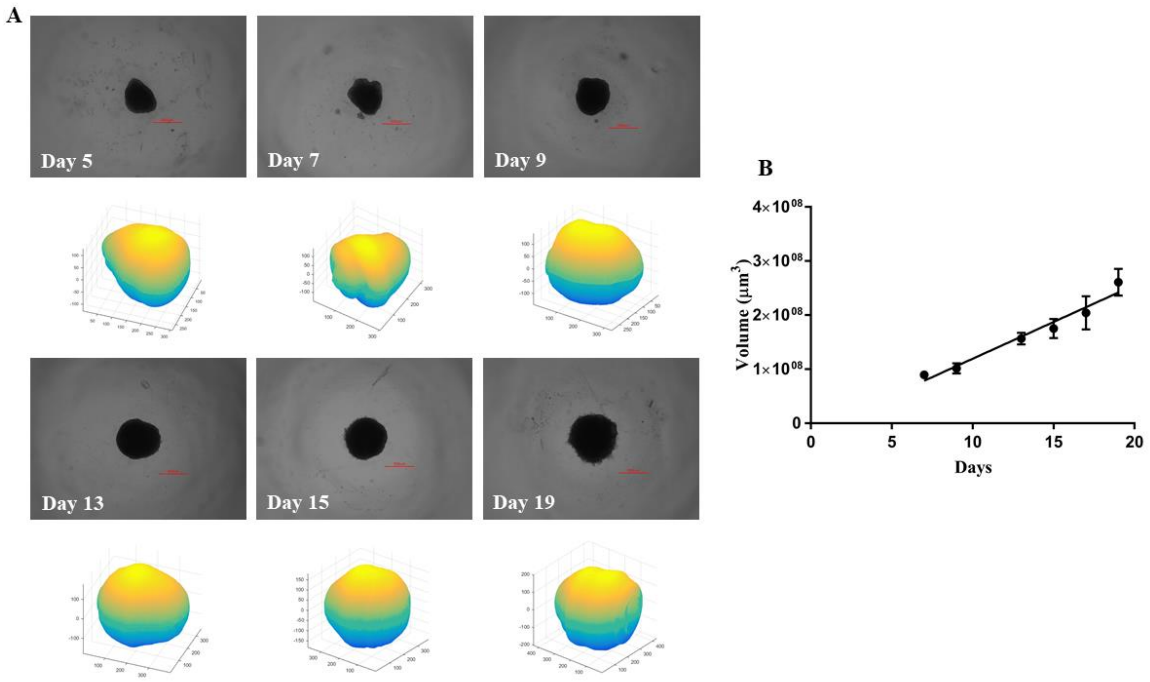

Figure 5: The morphology and volume of A549-iRFP MCS under brightfield microscope. (Mean±S.D, N = 6). (Scale bar=500μm).

2.3.3. Correlation between the fluorescence and the growth of A549-iRFP cells in MCS. In order to evaluate the capacity of the fluorescent signal of MCS to represent cancer progression, we also measure the fluorescent signal, volume and viability of MCS at different days. Similar to the monolayer results, the fluorescent signal has a strong proportional correlation with both the volume (R^2=0.9805, Fig. 6A) and the viability (R^2=0.9191, Fig. 6B) of MCS, indicating that the fluorescent signals of the A549-iRFP cells on the fluorescent imaging system would reflect the growth of A549-iRFP MCS *in vivo*.

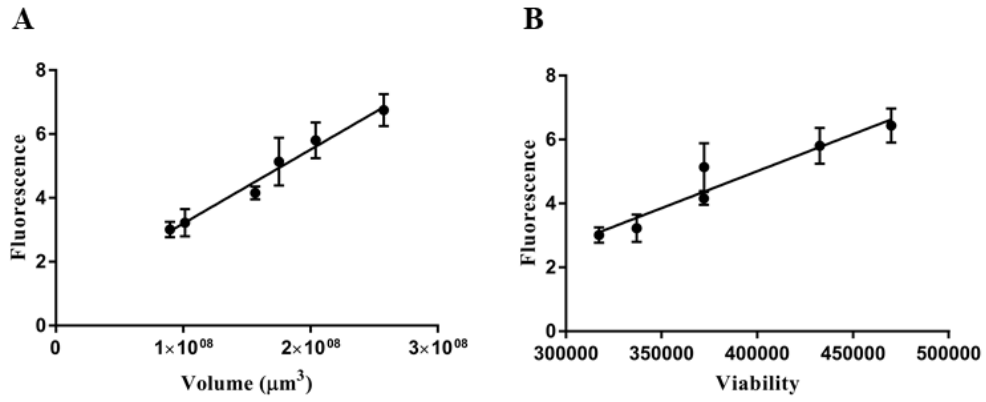

Figure 6: The cell viability and volume of MCS based on their bright-field images showed strong linear correlation with the fluorescent signal of MCS. (Mean±S.D, N = 6).

2.3.4. The morphology of A549-iRFP MCS showed rough and unclear edge after 15 days culture. The A549-iRFP MCS showed a round shape, tight structure and smooth surface in the first 15 days. As the culturing continued, the A549-iRFP MCS assumed rough edges on the surface, similar to the morphology of invasive cancers in the clinic. Moreover, some of the cancer cells were no longer tethered to MCS but dispersed into the culture medium. To define

and calculate the roughness of an MCS, we developed the equation: Roughness (mm) = (A_{OL}-A_{IL}) / L_{IL} [65], where A_{OL} is the area enclosed by OL, A_{IL} is the area enclosed by IL, and L_{IL} is the length of IL. As the culturing time increased, the roughness of MCS increased (Fig. 7).

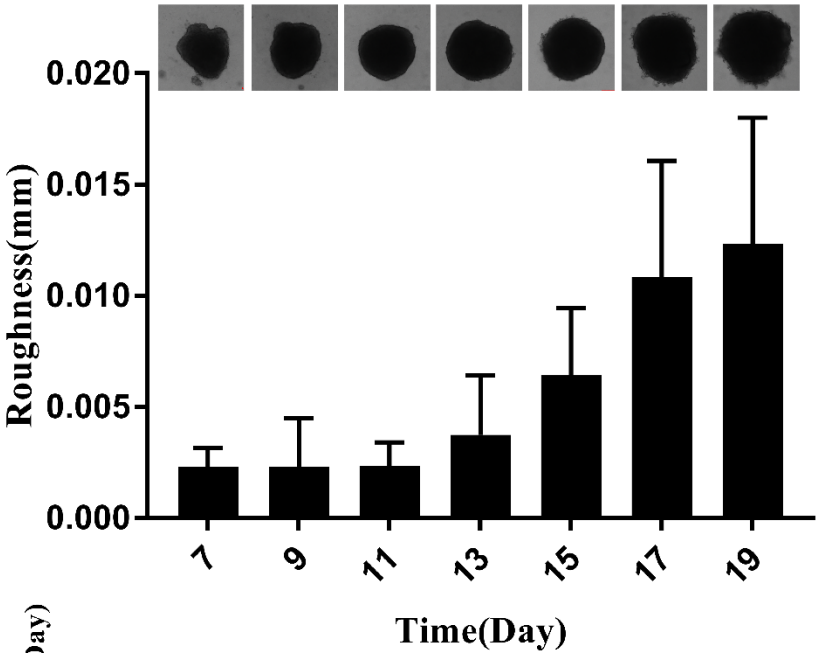

Figure 7: The roughness of A549-iRFP MCS increased with the culturing time. (Mean±S.D, N = 6).

2.3.5. Immunofluorescence imaging of live/dead cells showed a necrotic core in A549-iRFP MCS. In order to validate that the core of A549-iRFP MCS developed cell necrosis, we performed immunofluorescence staining using the Live/Dead cell viability assay. The green color (calcein-positive) represents live cells and the red color (ethidium-positive) represents dead cells. The plot of fluorescent intensity at two channels showed the heterogeneous distribution of live and dead cells in the A549-iRFP MCS. The images were taken 200 μm from the bottom of

the MCS. In the merged image, ethidium signal was stronger at the center of the MCS, which indicates accumulation of dead cells in the core. On the other hand, less live cells were shown by the calcein signal at the center of the MCS (Fig. 8). Taken together, the images demonstrate necrosis of cancer cells in the center of A549-iRFP MCS.

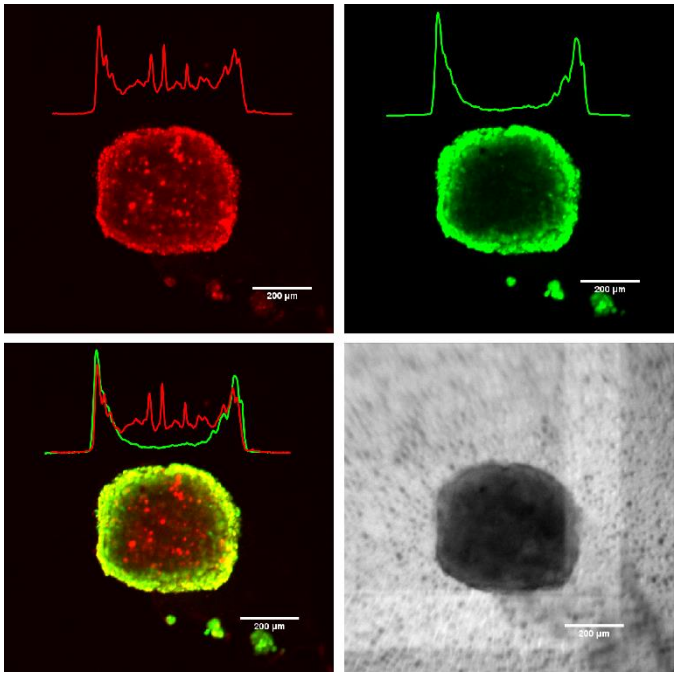

Figure 8: Immunofluorescence imaging confirms a core of necrotic cells in A549-iRFP MCS. (Scale bar=200 µm, N = 3)

2.3.6. Histological studies on the structure of A549-iRFP MCS using H&E staining.

To illustrate the tissue structure of A549-iRFP MCS, they were subjected to histological analysis. MCS were embedded in Paraffin three days, six days and twenty days after seeding and stained with Hematoxylin (blue) and eosin (red). Due to the size limitation of the samples,

MCS which were fixed at three days were cultured from cells that were seeded at 20000 cells/well density; MCS which were fixed at six days and twenty days were from cells that were seeded at 3000 cells/well density. The H&E staining reflected the basic tissue structure, where the blue color represents the nuclei and red color represents the cytoplasm.

The resultant images showed a very dense structure at the peripheral of MCS. Additionally, less nuclei were stained at the core of MCS. These observations confirm the presence of necrotic cells in the core of A549-iRFP MCS.

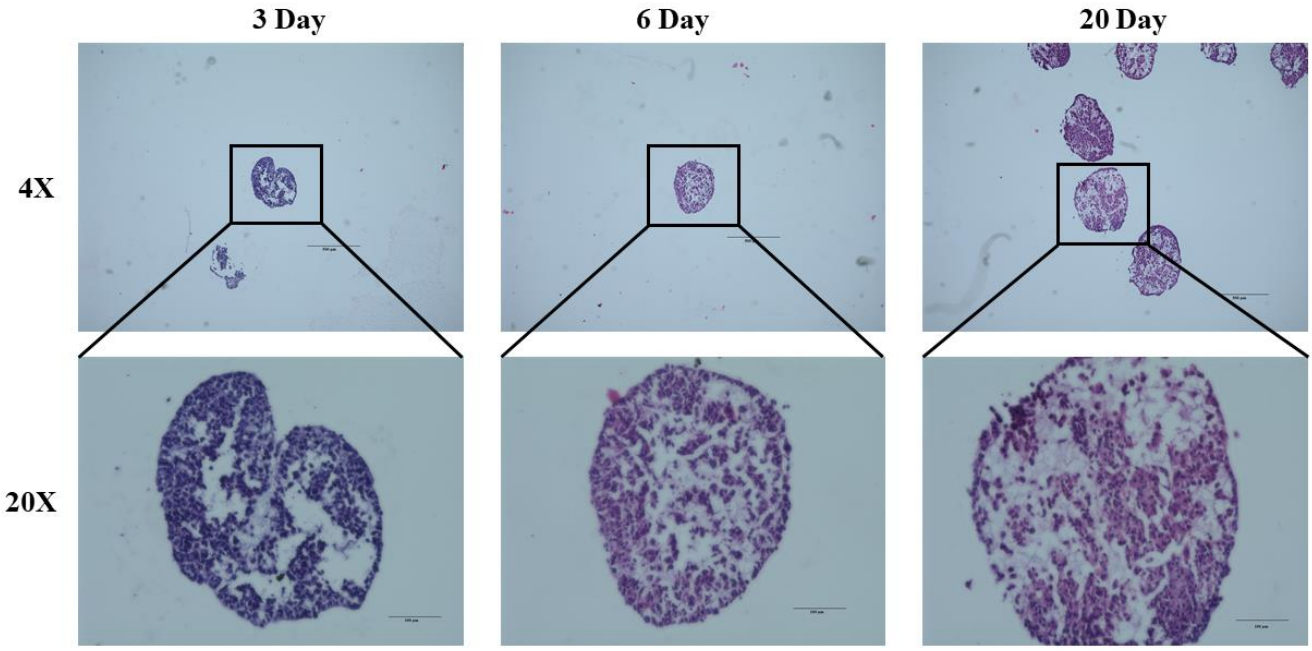

Figure 9: H&E staining of A549-iRFP MCS confirmed their necrotic core. (Scale bar=200 µm)

2.4 Discussion

3D MCS have been utilized not only in evaluating the therapeutic efficacy of drug candidates but also in studying the microenvironment of the solid tumor. In this chapter, the MCS that was constructed using A549-iRFP cells, which are human lung adenocarcinoma cells with stable fluorescent protein expression, showed a tight, round shape. The addition of 0.3% collagen into the culture media during the seeding process promoted the growth of MCS in low-attachment 96-well plates. The fluorescence from the stably expressed near-infrared protein iRFP was correlated strongly with the cell viability in monolayer, indicating that the fluorescent signal could represent the number of live cancer cells *in vivo*. Similarly, the fluorescent signal of A549-iRFP MCS was proportional to the spheroid viability, indicating that such fluorescent signal can be used to monitor the growth of live cancer cells *in vivo*.

The morphological change of A549-iRFP MCS from a smooth surface to a rough edge warrants our attention because it indicated that the peripheral cancer cells started to grow beyond the surface, to form a serrated edge, and to assume invasive growth. Because the local tissue invasion is the first step of cancer metastasis, the formation of the serrated edges on the MCS may represent the potential of cancer metastasis. We defined roughness to evaluate and quantify this morphological feature.

Such a morphological change probably resulted from the cell-cell interactions in the MCS. As cancer cells went through apoptosis in the necrotic core, they secrete many cytokines and chemokines into the extracellular matrix, such as those of the tumor necrosis factor (TNF) receptor superfamily. These cytokines and chemokines promote the cancer cells' invasion into the surrounding culture medium [66, 67].

The histology studies and the confocal immunofluorescence imaging confirmed the necrotic core inside the MCS. Due to the limited penetration of the photons, only images up to 200 μm depth from the bottom of the MCS showed acceptable resolution while images from deeper z-sections lost focus. In the merged images, the clear ethidium signal at the center of the core indicated the dead cells. Moreover, the H&E staining illustrated the inner structure of MCS after being cultured for different durations. A dense H&E staining of cancer cells at the peripheral of MCS and less nuclear staining in the core of the MCS validated the finding of a necrotic core by the confocal immunofluorescence imaging.

Chapter 3: Intrapulmonary Inoculation of Multicellular Tumor Spheroids to Construct an Orthotopic Lung Cancer Xenograft Model

3.1. Introduction

Ideally, mouse models for cancer should faithfully recapitulate the tumorigenesis, progression, invasion, and metastasis as well as predict response to treatment [68]. A broad category of mouse models, including xenograft, syngeneic, carcinogen-induced and genetically engineered mouse model (GEMM), have been developed to assist pre-clinical oncology research. In lung cancer research, GEMM precisely simulates the gene mutation and recaptures the histological feature of NSCLC. It is highly useful in studying tumorigenesis and genetic mutations in cancer development [35, 36]. However, the high cost in time and money of developing GEMM limits its application in evaluating therapeutics [25]. Xenograft mouse models allow quick *in vivo* assessment of a potential anticancer treatment (usually within 8 weeks), whereas GEMM takes a relatively long time. Moreover, the conditional GEMMs that rely on viral activation give rise to multiple tumor nodules in the lung, bypass the usual pattern of caner progression and metastasis, and induce early death of the animal [69].

Cell-line derived xenografts (CDX) represent the major type of animal model for use in anticancer drug development because of the mature technique and the relatively low cost. Most xenograft tumors have been developed subcutaneously because of the convenience in measuring the tumor growth. However, the rapid, non-indigenous growth of such tumors poorly reflects the microenvironment of the corresponding cancer in the clinic and does not meet the conditions for metastasis [15, 25]. In order to address this shortcoming, the orthotopic lung cancer xenograft has been developed by either injecting cancer cell suspension or implanting tumor graft in the lung. Although such cancer is developed in the organ of origin, the use of such methods can

cause extensive premature leakage at the injection site. Within five days, the cancer cells are found to spread to both sides of the lung, most probably due to the anatomy and respirational movements of the lung [43, 45, 48]. Therefore, this orthotopic model based on the injection of suspended cancer cells cannot adequately reflect cancer progression.

The surgical implantation of a tumor graft can potentially address issues of cancer cell leakage during pleural tumor seeding. Such a technique starts by harvesting the tumor which has grown subcutaneously in donor mice. The tumor is then cut into pieces, which were then transplanted into mice by surgically opening the chest. The models using this method carry meaningful advantages including a well-established solid tumor structure and a precise insertion site in the lung parenchyma. However, this method is technically difficult, needs a ventilator, and requires dedicated operators with the expertise. Moreover, high postoperative mortality of this method raises ethical concerns about the number of animals that are to be used [43].

Combining the advantages of transpleural injection and tumor graft implantation, we designed and developed a novel orthotopic lung cancer mouse model where MCS of fluorescent human lung cancer cells (A549-iRFP) were developed in culture and then inoculated into the left lung of mice. The MCS had a tight round morphology and a necrotic core, which reflected the essential characteristics of a solid tumor. This procedure enjoys high rates of postoperative survival (100%) and tumor establishment in/on the lung parenchyma (88.9%). The primary xenograft MCS mimicked the initiation of NSCLC, and progressed through distinct phases that closely mimicked all the four clinical stages of NSCLC over one month, and eventually spreads into both sides of the lung.

Table 1: Comparison of NSCLC Mouse Models.

	Implantation route	Tumor origin	Technical Feasibility	Natural Metastasis	Tumor Initiation	Capability of measure tumor growth	Tumor Growth Variation	Economical Adaptability	Reference
CDX	sc	Cell suspension	Easy	No	Single	Easy	Small	High	[43]
CDX	Orthotopic	Cell suspension	Easy	No	Multiple	Difficult	Small	High	[43, 47]
CDX	Surgical implantation	Tumor graft	Hard	No	Single	Difficult	Small	High	[43]
Experimental metastasis	iv	Cell suspension	Easy	No	Multiple	Difficult	Large	High	[50, 70]
Carcinogen induced	ip; iv; intratracheal	Carcinogen induced mutation	Easy	No	Multiple	Difficult	Large	High	[25, 71, 72]
PDX	sc	Tumor graft from patients	Easy	No	Single	Easy	Large	Low	[15, 25]
GEMM	Intratracheal; intranasal	K-ras activation	Easy	Distant metastasis	Multiple	Difficult	Medium	Low	[15, 25, 36]
GEMM	Intratracheal; intranasal	p53 inactivation	Easy	Distant metastasis	Multiple	Difficult	Medium	Low	[73]
CDX	**Orthotopic**	**Tumor spheroid**	**Easy**	**Intrathoracic metastasis**	**Single**	**Easy**	**Small**	**High**	

CDX: Cell line-derived xenograft; PDX: patient derived xenograft; GEMM: genetically engineered mouse model; sc: subcutaneous; iv: intravenous; ip: intraperitoneal;

3.2. Materials and Methods

3.2.1. Cell line and reagents. Human lung adenocarcinoma A549-iRFP was obtained from Imanis Life Sciences. A549-iRFP was cultured in DMEM growth media with 10% FBS, 1% pen/strep, and 1 µg/ml puromycin. 3D MCS were grown using 96 wells Spheroid Microplate from Coring life science. 20-gauge and 31-gauge needles were purchased from VWR. 100 µl Hamilton syringe was purchased from Fisher. BD™ U-100 Insulin Syringe 31-gauge × ½ was purchased from Patterson Veterinary (USA). Surgical instruments were purchased from Fisher and Fine Science Tool. Matrigel was purchased from Corning Life

Science. Ketamine, Xylazine, and Isoflurane were obtained from Patterson Veterinary (USA). Ophthalmic ointment, Buprenorphine, and Antibiotic ointment were purchased from Patterson Veterinary (USA).

3.2.2. Animals. 5 to 6 weeks old male Athymic Nude Mice were purchased from Simonsen Labs Inc (CA, US). All mice were fed with AIN-93M Mature Rodent Diet from Research Diet (NJ, US). The *in vivo* study was performed based on the animal protocol (No. 18R01) which was approved by the Institutional Animal Care and Use Committee (IACUC), University of the Pacific. The mice (5-6 weeks old) were kept in sterilized cages and provided with sterilized rodent diet and water, and under controlled lighting cycle. The mice were allowed to acclimate to the environment for one week in the facility before the start of the experiment.

3.2.3. Construction of MCS using A549-iRFP cell. A549-iRFP cells were seeded in the 96-well spheroid plate at the density of 4000 cells/well. MCS were developed with the methods described in Chapter 2. The MCS were generally cultured for 19 days, when the rough edge of MCS could be observed, MCS were transferred into a petri dish with ice cold PBS ready for inoculation.

3.2.4. Injection of cell suspension into the left lung of mice. Nine mice were anesthetized by an intraperitoneal injection of anesthesia cocktail (Ketamine 100 mg/kg, xylazine 15 mg/kg). After sterilizing the skin, a 0.5 cm incision was made at the tail-side of the left scapula. The muscle and fat were gently separated with forceps to expose the rib bone. After visualization of the motion of the left lung, a 31-gauge needle-attached syringe, which contained 1×10^6 A549-iRFP cancer cells suspended in a 50 μl mixture of PBS and Matrigel (PBS: Matrigel = 1:1) was injected into the left lung parenchyma through the sixth intercostal space at a depth of

~3 mm of eight mice. One mouse was injected with a 50 μl mixture of PBS and Matrigel (PBS: Matrigel = 1:1) without A549-iRFP cells.

3.2.5. Inoculation of MCS into the mice lung. To inoculate MCS, A549-iRFP cells were first cultured into MCS of desirable morphology (size, roughness) as defined in prior sections. MCS were transferred into 5 mL ice-cold PBS in a sterilized Petri dish (60 mm ×15 mm). Twenty mice were anesthetized by an intraperitoneal injection of anesthesia cocktail (Ketamine 100 mg/kg, xylazine 15 mg/kg). After sterilizing the skin, a 0.5 cm incision was made at the tail-side of the left scapula. The muscle and fat were gently separated with forceps to expose the rib bone. One 20-gauge needle attached to a 100-μl syringe was used to first take up 20 μl mixture of PBS and Matrigel (1/1 in volume) on ice, and then to take up one MCS in minimal volume of PBS in order to keep the MCS inside the needle but not in the syringe. The needle was then inserted into the lung through the sixth intercostal space, followed by slow injection of the MCS into the left lung of eighteen mice. Two mice were inoculated 20 μl mixture of PBS and Matrigel (1/1 in volume) without MCS. The wound was then treated with triple antibiotic and sealed with a surgery clip, which was removed seven days later.

3.2.6. *In vivo* fluorescent imaging of lung cancer progression. Animals that had been inoculated with suspended A549-iRFP cells or MCS were imaged every three days on a Pearl® Trilogy small animal imaging system and an Odyssey® Infrared Imaging 205 System at the 700 nm channel. Animals for imaging on the Pearl® Trilogy system took postures of four directions - left, right, ventral and dorsal. Animals were maintained under anesthesia by breathing isoflurane.

The tumor growth after MCS inoculation was quantified from the left-posture images using the Image Studio Lite Ver 5.2 software. For each image, the fluorescent intensity within a

rectangle (height × width = 176 × 107) that covered the thoracic cavity was recorded as the gross cancer fluorescence and then subtracted by the fluorescent intensity within a rectangle (height × width = 24 × 44) that covered the left thigh as the background from autofluorescence. The mean and SEM of six mice are reported.

3.2.7. Open-chest anatomy and *ex vivo* imaging. After animal sacrifice by anesthetic overdose, the thorax was carefully opened with a midline incision. The diaphragm and the lateral chest walls were then removed to expose the lungs and to confirm the location of the xenograft tumor, which possessed a lighter color than the surrounding tissue. A 25-gauge needle attached to a syringe was used to make a cardiac puncture and to inject 5 mL PBS into the right cardiac ventricle in order to flush the lung vasculature. The lung was then carefully dissected from the chest and washed with ice-cold PBS before being transferred onto the Pearl® Trilogy system for imaging at the 700 nm channel.

3.2.8. Lung fixation. Mice in stage 4 of NSCLC were euthanized by anesthetics overdose. The ventral side of the trachea was surgically exposed, and a small cut was made to insert a 20-gauge needle tip. Upon insertion, the needle tip was tied to the trachea with a suture. The thorax was carefully opened with a midline incision to expose the lungs. The right cardiac ventricle was injected with 5 mL of PBS to flush the lung vasculature using a 25-gauge needle. The needle in the trachea was then infused with 2 to 3 ml 4% formaldehyde in PBS (Fisher Scientific, US) to inflate the lung. After 20 minutes the lung was carefully dissected and immerged in formaldehyde overnight.

3.2.9. Histological analysis of fixed lung tissue using H&E staining. The lung tissue from healthy mice, mice injected with suspended cancer cells, and mice inoculated with MCS were subjected to histology studies. After fixation, the lung tissues were embedded with

paraffin, cut into 5 μm-thick sections by an HM 325 Rotary Microtome, and stained with H&E for microscopic imaging on a Keyence (US) BZ-X700 fluorescence microscope.

3.3 Results

3.3.1. Postoperative mortality rate and tumor establishment rate. The MCS were cultured long enough to display rough edges before the inoculation, minimal volume of liquid and needle size were used to transfer the MCS, and the needle was filled with a 20 μl of Matrigel before the uptake of the MCS so that it can be inoculated sufficiently deep into the lung tissue. After such procedural optimization, the survival rate after A549-iRFP MCS inoculation reached 100% (18/18), compared to 87.5% (7/8) survival rate after injecting the suspended A549-iRFP cells by our hands. The *in vivo* fluorescent imaging and anatomical observation were carried out to confirm the successful inoculation of MCS. All mice injected with cell suspension developed cancer in 3 to 6 days as shown by fluorescent signals from both sides of the lung (7/7). Among mice inoculated with MCS, 88.9% (16/18) of the animals either clearly displayed tumor nodule on the left lung by anatomical observations or eventually showed cancer metastasis to both sides of the lung by *in vivo* fluorescent imaging (Table 2).

Table 2: Postoperative Mortality Rate and Tumor Establishment Rate.

	Cell suspension	**MCS**
Postoperative survival rate	87.5%	100%
Tumor establishment rate	100%	88.9%

3.3.2. Rapidly increasing fluorescent signal in both sides of the lung indicates a severe leakage of cancer cell suspension 3 days after injection. Within 3 days, the fluorescent signal was seen in both sides of the lung in mice that were injected with the A549-iRFP cell suspension (Fig. 10), which indicated the premature leakage of cell suspension from the injection site. Further, the fluorescent signal was stable from 9 days to 30 days after the injection of suspended cancer cells failing to reflect the cancer progression in clinic. After euthanasia and opening the chest, massive tumor aggregates were seen floating inside the thorax. The minimum survival days for mice after injection of cancer cell suspension is 5-6 weeks, most probably due to the heavy tumor burden.

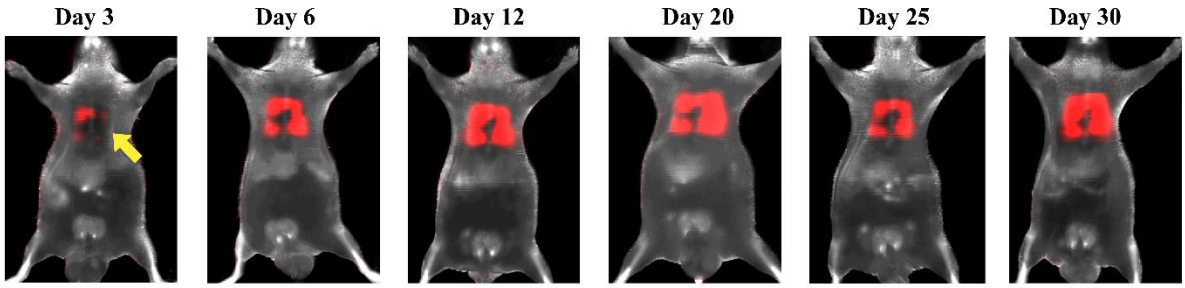

Figure 10: The in vivo imaging of mice injected with A549-iRFP cell suspension. The red color from the 700 nm channel represents the cancer cells. The grey color from the 800 nm channel represents the body autofluorescence. (N = 7)

3.3.3. *In vivo* fluorescent imaging of cancer progression in MCS-inoculated mice.

After MCS inoculation, the development of the corresponding xenograft tumor was monitored by fluorescent imaging on both the left side and the ventral side. Between 3 and 9 days after the surgery, condensed fluorescence in the left lung was observed, indicating the establishment of a localized tumor in the left lung that mimicked Stage 1 NSCLC in clinic. Between 9 and 15 days after surgery, the fluorescence substantially increased in intensity and/or split to multiple locations in the left lung, indicating the presence of tumor(s) that mimicked Stage 2 NSCLC in clinic. The fluorescent signal detected from the ventral side imaging kept increasing, suggesting a Stage 3-like development of the xenograft. At about 21 days after the surgery, perfused fluorescence was detected on both sides of the lung, indicating the metastasis of the cancer, which mimicked the Stage 4 NSCLC in clinic (Fig. 11).

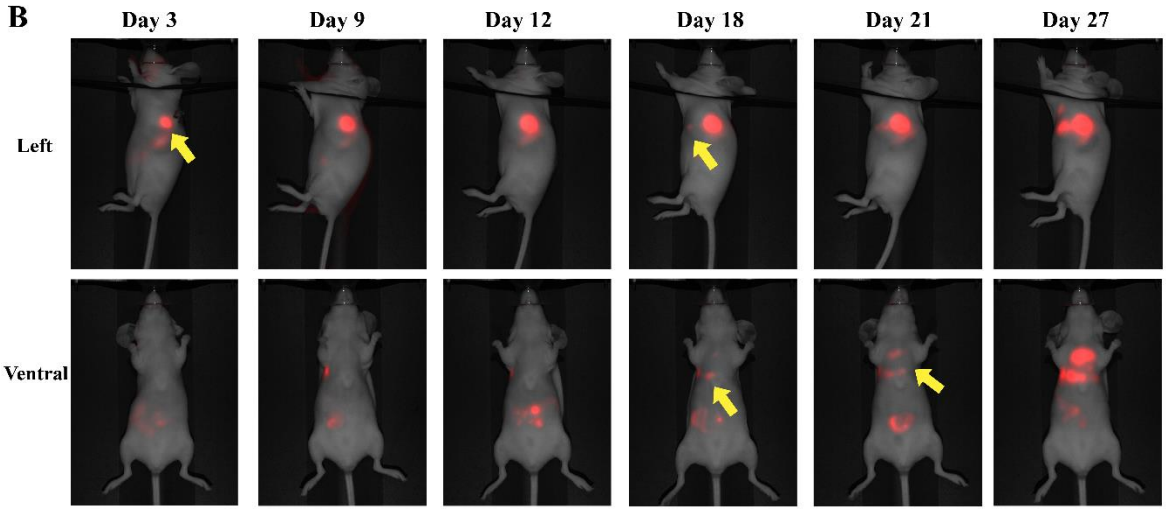

Figure 11: In vivo imaging of MCS-inoculated nude mice. The left side (Inoculation side) and ventral side of nude mice were detected using Pearl® Trilogy Small Animal Imaging System at 700 nm channel. The yellow arrow indicates the tumor location, cancer growth and metastasis are based on the fluorescent signal. (N = 9)

3.3.4. Characterization of MCS-inoculated mice by ex vivo fluorescent imaging and anatomical observation. To further characterize the xenograft cancer progression, three mice were sacrificed 8, 11, 18, and 27 days after MCS inoculation followed by open-chest anatomy and *ex vivo* fluorescent imaging of the dissected organs (Fig. 12). Both the anatomy and the *ex vivo* fluorescent imaging showed that the tumor was confined in the inoculation site at day 8, which mimicked a primary solid tumor at Stage 1 NSCLC. On day 11, the increase of fluorescent signal indicated tumor growth in the left lung, reminiscent of Stage 2 NSCLC. On day 18, both the anatomy and the *ex vivo* fluorescent imaging showed confined tumor growth in the left lung. The anatomy and the *ex vivo* imaging also detected tumor growth on the surface of the heart, which is a key indicator for Stage 3 NSCLC in clinic. As further validation, the *in vivo* and *ex vivo* fluorescent images were highly correlated in showing the shape and location of the tumors. Interestingly, fluorescent lymph nodes were not clearly observed on day 18, which could be attributed to the immune deficiency of the nude mice. On day 27, the fluorescent imaging showed heavy tumor burden whereas the open-chest anatomy showed perfuse tumor growth in both sides of the lung, the heart, the trachea, and the major blood vessels, demonstrating the cancer metastasis that mimicked Stage 4 NSCLC.

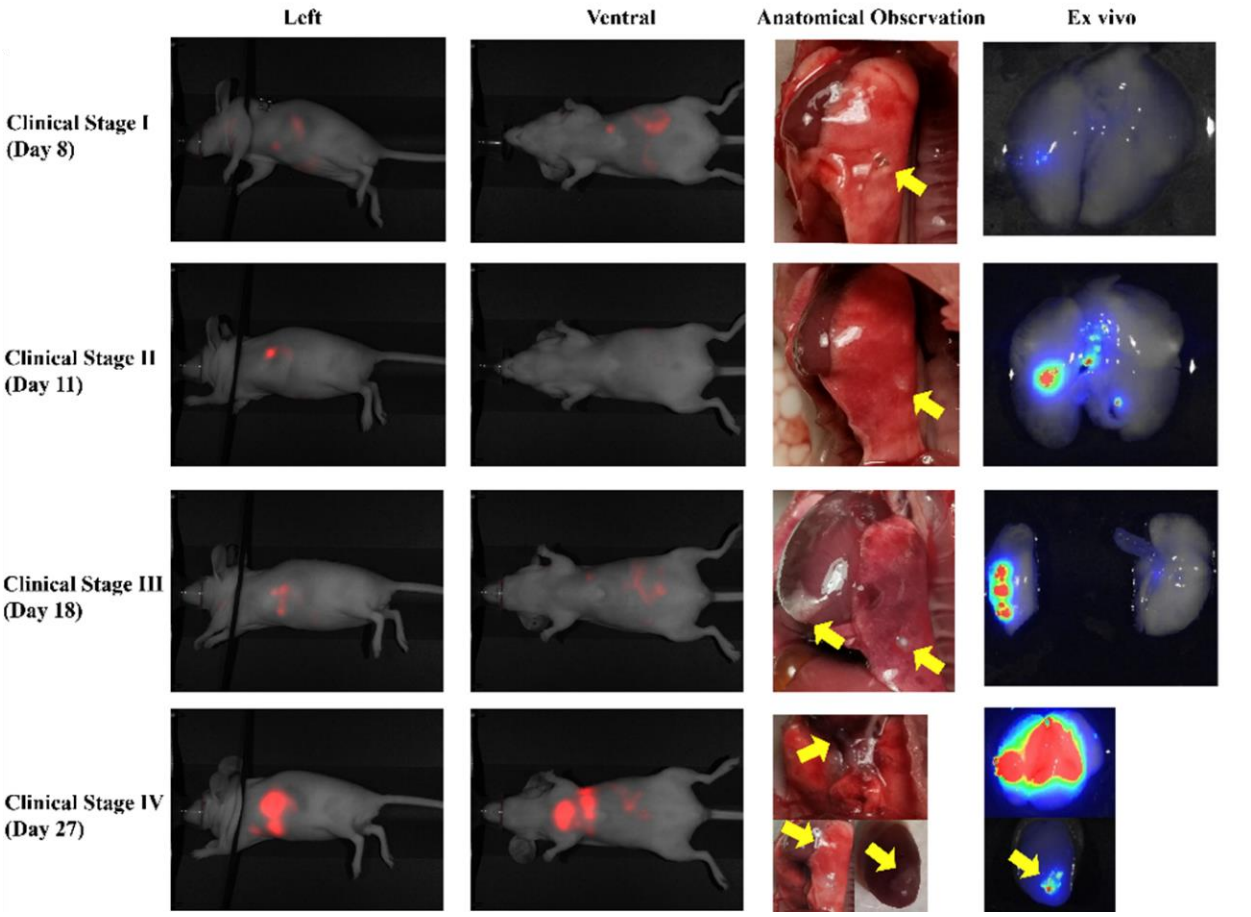

Figure 12: Cancer progressed through four clinical-like stages in the MCS-inoculated mice model. Mice that were inoculated with MCS were euthanized at day 8, 11, 18 and 27 later. The ex vivo imaging and anatomical observations showed the tumor growth and indicate the cancer progressed in all the four stages. The yellow arrow points out the tumor on lung and heart. (N = 3)

3.3.5 Effects of MCS morphology on the time needed to develop cancer metastasis in the thorax. The fluorescence of iRFP was used to semi-quantitatively monitor the tumor growth and cancer progression. Specifically, the left-posture images were analyzed, where the fluorescent intensity within the same shape of rectangle that covered the thorax of the mouse for each image was used to represent the gross signal of the cancer cells. This number was then subtracted by the fluorescent intensity within another rectangle that covered the left thigh of the

mouse to be corrected for the body autofluorescence. The corrected fluorescent intensity was recorded over time to represent the tumor growth. As shown in Fig. 13A, the tumor growth was relatively slow and stable in the first 20 days but accelerated afterwards, indicating a quicker proliferation of cancer when the tumor reached a larger size.

To improve the consistency of the lung cancer model under our study, we explored possible correlations between morphological features of the inoculated MCS and the pace of cancer progression after inoculation. Several morphological features of each A549-iRFP MCS were recorded right before inoculation, including the fluorescent signal, the volume, and the roughness. The roughness was defined by the equation, Roughness (mm) = $(A_{OL}-A_{IL}) / L_{IL}$, where A_{OL} is the area enclosed by OL, A_{IL} is the area enclosed by IL, and L_{IL} is the length of IL. The time when the fluorescent signal was first detected in both sides of the lung after inoculation was also recorded as the time needed to develop metastatic cancer that mimicked Stage 4 NSCLC. The Roughness of MCS right before inoculation (Fig. 13B, $p=0.0299$, $R^2=0.5134$), but not the fluorescence (Fig. 13C, $p=0.9915$, $R^2=0.00012$), nor the volume (Fig. 13D, $p=0.837$, $R^2=0.00647$), was associated significantly with the time needed to develop metastatic cancer. Specifically, the higher the value of roughness, the less the time needed to reach metastasis.

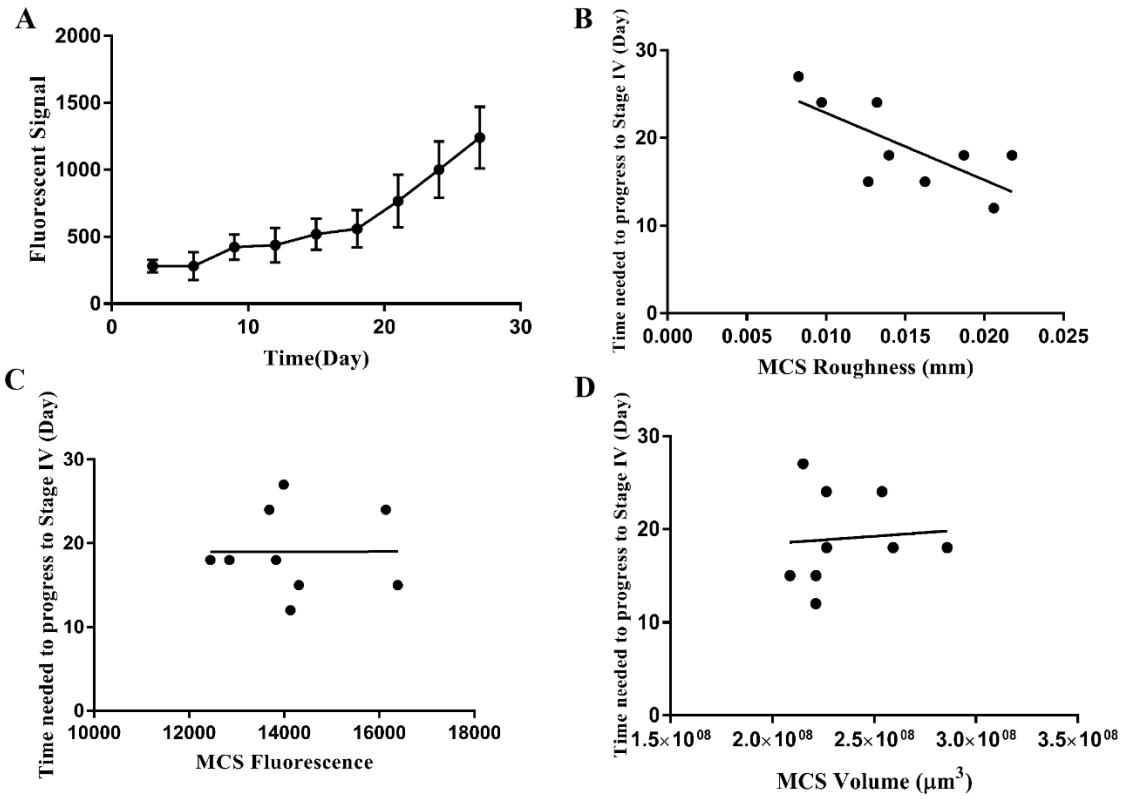

Figure 13: The morphology of MCS influence the time needed for cancer metastasis to both sides of the lung. (A) Quantitation of tumor growth over time by the fluorescent intensity at thorax (large rectangle) subtracted by the background fluorescent intensity at the left leg (small rectangle). (Data are mean±SEM, n=6). The time needed to develop into metastasis correlated with the roughness (B, $p<0.05$, N=9) of the inoculated MCS but not the fluorescent intensity (C) nor the volume (D).

3.3.6. Histological analysis of lung tissues after MCS inoculation. Post-metastasis mice were dissected to isolate the lungs for histological studies using the hematoxylin and eosin (H&E) staining to visualize the lung and the tumor tissue structure (Fig. 14). Lung tissues from mice inoculated with A549-iRFP MCS showed a dense, round nodule surrounded by thin-walled alveoli, confirming that the MCS was successfully established inside the lung parenchyma. In comparison, lungs from mice injected with A549-iRFP cells in suspension showed massive and

dense tumor tissue that occupied the majority of the lung, confirming the perfusion of cancer cells as indicated by fluorescent imaging. As the healthy control, mice without cancer cell inoculation gave normal lung tissue consisting only of thin-walled alveoli and bronchiole with ample air space.

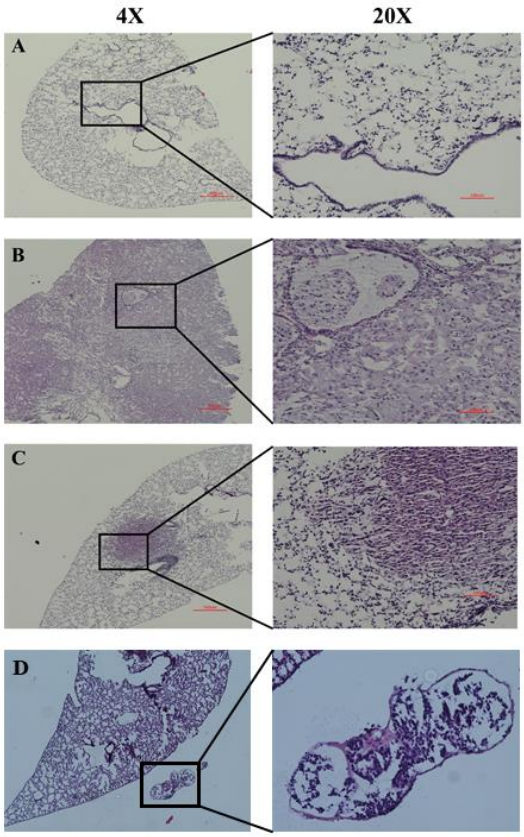

Figure 14: Histological imaging of mice lung tissue after H&E staining. (A) Healthy lung tissue. (B) The lung tissue of mice that injected with cancer cell suspension. (C-D) The lung tissue of mice that inoculated with MCS. (Scale bar=500μm)

3.4 Discussion

This Chapter reports a novel orthotopic lung cancer model based on intrapulmonary inoculation of MCS made of human lung cancer cells. The xenograft MCS progressed through distinct phases that closely mimicked all the four clinical stages of NSCLC. The progression lasted about one month, which is a commonly used time frame to evaluate anticancer drugs in animal models. In comparison with the cell suspension injection methods, the MCS better mimiced the condensed morphology of primary solid tumors that presents a barrier for drug penetration. The MCS inoculation also prevented the leakage and the pleural seeding problems that are common in the xenograft lung cancer models based on injection of a cancer cell suspension. Compared with GEMM, this model carries the advantage of starting with only one solid MCS per animal, a light burden of lung cancer to enhance the long-term survival of the animals after surgery. Therefore, the novel model described herein opens many doors to evaluate anticancer agents that could be developed to treat different stages of lung cancer in the clinic.

Starting from the *in vitro* construction of MCS using commercially available human lung cancer cell line A549-iRFP, it took about three weeks to culture hundreds of MCS on 96-well plates for the inoculation, similar to the time needed to culture enough suspended cells for common mouse models of tumor xenografts. Each MCS inoculation took about 20 minutes, which allowed one experienced researcher to inoculate 20 mice per day. After establishing the correlation between the fluorescence and the viability of A549-iRFP cells and their MCS, the progression of the xenograft lung cancer can be conveniently imaged because of the low tissue absorbance of the infrared fluorescence and the low body autofluorescence at the same wavelength. For each posture of the mouse, imaging at two different wavelengths took only 30

to 40 seconds to complete, much shorter than the time needed for CT/PET scans. Overall, the efficiency and low cost of the new lung cancer model would favor its large-scale use in preclinical drug development.

Large variations in tumor growth between individual animals represents a significant challenge in animal cancers models. For example, xenograft tumors from inoculation of suspended cancer cells can differ largely in size due to variations in the volume of the cancer cell suspension that actually retains at the injection site. Differences in the tissue disruption between injections could also lead to differences in the settlement of the inoculated cells, and thus in the resultant tumor shape. In this study, efficient culturing allowed us to select MCS of highly consistent size, density, shape, and roughness so that the following cancer development was more consistent. The significant correlation between the roughness of the MCS and the time needed for metastasis further suggest that the progression of lung cancer in this model could be well controlled by monitoring the morphological features of the MCS.

One limitation of this model is that occasionally the xenograft tumor was developed on the surface of the lung rather than inside the lung parenchyma. This problem is probably due to the relatively thick 20-gauge needles that sometimes did not penetrate the lung tissue during inoculation. The following is a possible solution to this deviation. First, a smaller but more aggressive MCS can be cultured and inoculated into the lung. 20-gauge needles with a 610 μm inner diameter can pick up MCS with diameter around 750 μm. Therefore, a smaller needle can be utilized to inoculate the smaller MCS into the lung parenchyma, such as a 25-gauge needle with a 500 μm inner diameter. To construct such smaller and more aggressive MCS, we are currently developing MCS that consist of lung cancer cells and fibroblast cells.

Another limitation of this model at its current stage of development is the lack of metastasis to remote organs. Although brain and liver are two major sites of lung cancer metastasis in clinic, no significant fluorescence increase was detected in these organs during the course of our studies. This was probably due to the athymic mice's partial immune function, which would clear the A549-iRFP cells from blood circulation before any invasion into brain or liver tissues.

Chapter 4: *In Vitro* Characterization of Co-Culturing MCS that Consist of A549-iRFP Cell with WI38 Fibroblasts

4.1. Introduction

Drug resistance, lethal metastasis and cancer recurrence are the key issues in cancer [74]. Recent investigations have shed light on the tumor microenvironment (TME) that can potentially impose these challenges and thus hampers the prognosis of many types of cancer. TME is composed of various stromal cells, including fibroblasts, macrophages, endothelial cells and lymphocytes, which are surrounded by the extracellular matrix (ECM) [8]. Cancer-associated fibroblasts (CAFs) are one of the abundant stromal cells in the TME, especially in solid tumors.

Normally fibroblasts cells remain quiescent until being activated to reactive fibroblasts during the wound-healing process. In TME, the tumor has been recognized as a wound that does not heal, which is thought to keep the fibroblasts activated. Moreover, hypoxia and oxidative stress inside the solid tumors further stimulate the local fibroblasts. Therefore, TME can re-educate normal fibroblasts into CAFs [75].

Numerous animal and cell culture studies have demonstrated that CAFs can promote cancer progression, invasion, metastasis, and drug resistance [76]. The high capacity of CAFs in synthesizing ECM proteins such as collagens, fibronectins and laminins helps remodel the TME to support cancer cell growth [77]. Moreover, by secreting cytokines and chemokines, CAFs promote tumor progression in many aspects including tumorigenesis, angiogenesis and metastasis. For example, inoculation of activated fibroblasts with human mammary epithelial cell in mice have been shown to boost neoplasia. For another example, the overexpression of transforming growth factor beta (TGF-β) and hepatocyte growth factor (HGF) by CAFs facilitate tumorigenesis [78]. CAFs can also recruit endothelial cells by secreting stromal cell-derived

factor 1 (SDF1) to promote the formation of new vasculature, which supplies oxygen and nutrition for the cancer cells [79]. CAFs also foster cancer metastasis in multiple steps. Chemokines that are secreted by CAFs, such as SDF1, promote breast cancer metastasis to bone marrow [80]. Notably, tumor never metastasized in fibroblast-deficient mice [81].

Co-culturing of SV80 cells (human fibroblasts) with A549 MCS enhanced the adherent tissue structure, elevated the hypoxic condition and promoted the epithelial-to-mesenchymal transition (EMT) [82]. This result suggests that MCS from co-culturing cancer cells with fibroblast cells would generate a more relevant TME to promote tumor growth. Another study showed that WI38 human lung fibroblasts could be re-educated to CAFs by indirect co-culturing with A549 monolayer cells. The re-educated WI38 promoted the invasion of A549 cells in a transwell assay [10]. Therefore, we have selected the WI38 fibroblast cells as the stromal cells to be co-cultured with A549-iRFP in order to construct more aggressive MCS.

4.2. Material and Methods

4.2.1. Cell line and reagents. A549-iRFP cancer cells were cultured as reported in Section 2.2.1. The human lung fibroblast cell line WI38 was obtained from ATCC. WI38 was grown in EMEM (Corning Life Science, US) cell culture medium with 10% FBS, 1% Penicillin-Streptomycin, and additional L-glutamine. Falcon® 96-well Black/Clear Flat Bottom Microplate and 96-well Spheroid Microplate were purchased from Coring life science. M-PER™ Mammalian Protein Extraction Reagent was purchased from Thermo Fisher. Hoechst 33342 was purchased from Thermo Fisher. The α-Smooth Muscle Actin antibody and Anti-Mouse IgG2a (γ2a)-CF™568 antibody were purchased from Sigma-Aldrich. 4% formaldehyde in PBS was purchased from Fisher Scientific for fixation. Paraplast was purchased from Sigma

(St. Louis, MO) for tissue embedding. Hematoxylin and Eosin were purchased from VWR International, (Radnor, PA).

4.2.2. Co-culture of A549-iRFP with WI38 cell in monolayer. A549-iRFP cancer cells and WI38 lung fibroblast cells were seeded in 6-well microplates at ratios 1:1 and 1:2. After reaching 80% confluence, the cells were lysed with the M-PER protein extraction buffer. The total protein was extracted and centrifuged at 14000 × g for 10 mins. The supernatant was transferred into a black wall 96-well plate with 100 µl per well, each group have 6 replicates. The fluorescent signal was measured under Odyssey® Infrared Imaging 205 System (Channel:700nm).

4.2.3. Construction of co-culture 3D MCS using A549-iRFP and WI38 cells. The MCS were cultured as described in Sections 2.2.3. Co-culture MCS were constructed at different ratios of cancer cells to fibroblast cells (A549-iRFP:WI38 = 4000:4000, 4000:2000, and 4000:500). The seeding density of A549-iRFP cells was 4000 cells/well. The fluorescent signal was measured by Odyssey® Infrared Imaging 205 System (Channel: 700 nm), and the morphology of MCS was observed under Keyence fluorescence microscope BZ-X700. The roughness of MCS was calculated using the equation: Roughness (mm) = $(A_{OL}-A_{IL}) / L_{IL}$, as in Chapter 2

4.2.4. Immunofluorescence study on co-culture monolayer cells. Cancer cells and fibroblast cells were seeded in 6-well microplates in different groups: A549-iRFP cells only, WI38 cells only, A549-iRFP:WI38 = 1:1, A549-iRFP:WI38 = 1:2, and WI38 cells with conditional medium. WI38 cells were cultured with the conditional growth medium, which was changed every day. The conditional growth medium was prepared by mixing the medium from the A549-iRFP cells only group and that from the WI38 cells only group at 1:1 ratio, followed by

centrifugation of the mixture at 500 × g. The resultant supernatant was then stored at -20 °C as the conditional growth medium. After five days in culture, the different cell groups were fixed with 4% formaldehyde in PBS for 10 min at room temperature and washed with PBS three times. The cells were then permeabilized by incubation for 10 min with PBS containing 0.25% TritonX-100. The cells were then washed in PBS three times and incubated with 5% milk powder in PBST (PBS with 0.1% Tween 20) for 30 min to block non-specific binding. The cells were then incubated with the 5 µg/ml primary antibody (Anti-Actin, α-Smooth Muscle antibody, Mouse Monoclonal) in PBST with 1% milk powder for 1 hour at room temperature. The antibody solution was decanted and the cells were washed three times in PBS, 5 min each wash. The cells were then incubated with the secondary antibody for 1 hour at room temperature. The antibody solution was decanted and the cells were washed with PBS three time for 5 min each in darkness. The cells were then incubated with 1µg/ml Hoechst 33342 for 5 min in darkness at room temperature and washed with PBS three times before imaging. The images were recorded using Keyence fluorescence microscope BZ-X700 (λ_{ex}=361 nm, λ_{em}=486 nm for Hoechst, λ_{ex}=562 nm, λ_{em}=583 nm for α-SMA).

4.2.5. The live/dead imaging of co-culture MCS by confocal microscopy. MCS were cultured in 96-well spheroids microplate until the diameter reached 500 µm. MCS were transferred to a glass bottom Petri dish and incubated with a LIVE/DEAD™ Cell Imaging Kit (ThermoFisher, US) for 45 minutes at 37 °C. The MCS were washed with PBS 3 times after incubation and imaged under Leica DMIRE2 confocal microscope (λ_{ex}= 491 nm, λ_{em}= 513 nm for live cell, λ_{ex}= 561 nm, λ_{em}= 607 nm for dead cell). Images were analyzed using the ImageJ software.

4.2.6. Immunohistochemistry (IHC) and H&E staining of co-culture MCS. The protocol of paraffin-embedding and histology staining were described in Section 2.2.6. A549-iRFP and WI38 cells were seeded at 1:1 ratio on the 96-well spheroid microplate. The histology section was de-paraffined using Safeclear II and rehydrated with different concentrations of alcohol. The H&E staining method was described in Section 2.2.6. The immunofluorescent staining protocol was described in Section 4.2.4. The slides were incubated with 5 μg/ml primary antibody (Anti-Actin, α-Smooth Muscle antibody, Mouse Monoclonal) overnight at 4 °C instead of 1 hour at room temperature.

4.3. Results

4.3.1. Co-culturing with WI38 fibroblasts promoted proliferation of A549-iRFP cells in monolayer. The fluorescent signal of A549-iRFP cells can represent the cell viability as we showed in Chapter 2. We utilized the fluorescent intensity to semi-quantify the number of cancer cells in co-culture with WI38 fibroblasts. The fluorescent signal was measured using the Odyssey Infrared Imaging 205 System at 700 nm channel. Each well was monitored under the microscope to ensure the cell confluence was under 80% before extracting the total protein. The results showed a significant difference in the A549-iRFP cell alone and the co-culture (1:1) group (Fig. 15, $p=0.0095$, $N=6$, mean$\pm$SD).

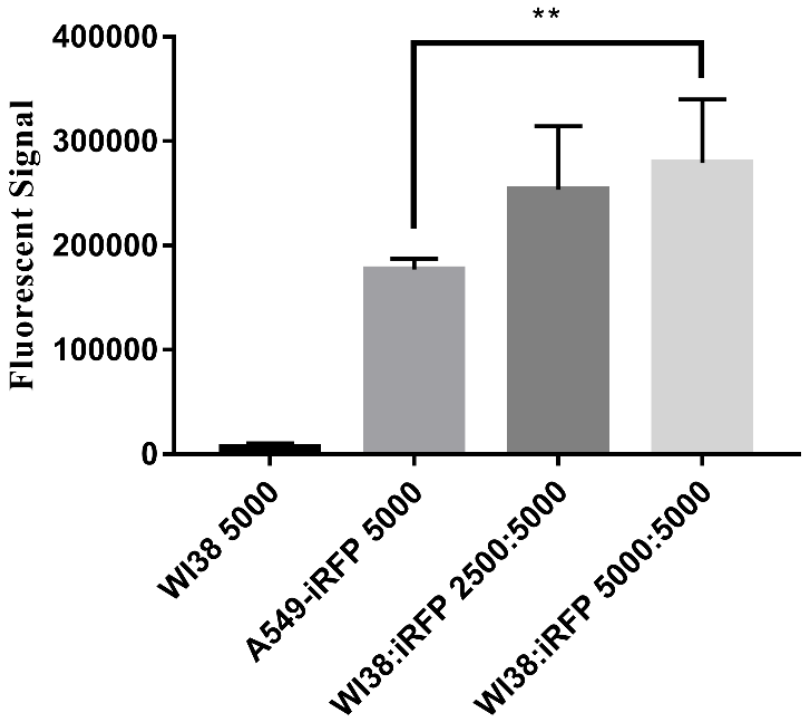

Figure 15: Increased growth of A549-iRFP cells after being co-cultured with WI38 fibroblasts. (Mean±S.D, N = 6)

4.3.2. Elevated expression of α-SMA indicated that WI38 fibroblasts were re-educated to cancer-associated fibroblasts. Cancer-associated fibroblasts (CAFs) are characterized by the upregulated expression of α-smooth muscle actin (α-SMA). It has been reported that normal fibroblast cells WI38 can be activated to CAFs after being co-cultured with A549 cells. The relatively high expression of α-SMA was illustrated by immunofluorescence and western blot. Therefore, we utilized α-SMA as the biomarker to validate that A549-iRFP cells could also re-educate normal fibroblasts to CAFs (Fig. 16). After co-culturing at different seeding densities for 5 days in the 6-well plate, the monolayer A549-iRFP cells were fixed by

4% formaldehyde followed by immunofluorescence. The red color represents the expression of α-SMA which was read at 568 nm on Keyence fluorescence microscope BZ-X700. The nucleus was stained with Hoechst which read at 405 nm to locate the cells. The immunofluorescence assay revealed that WI38 cells that had been co-cultured with A549-iRFP cells expressed a higher level of α-SMA compared with WI38 cells alone. Moreover, WI38 which had been cultured with conditional medium also had a positive expression of α-SMA. To semi-quantify the α-SMA expression, the grey value of 6 cells at 568 nm in each image was quantified using the ImageJ software (Fig. 17). The co-culture group and conditional medium group showed a significant increase of α-SMA expression compared with WI38 cells alone.

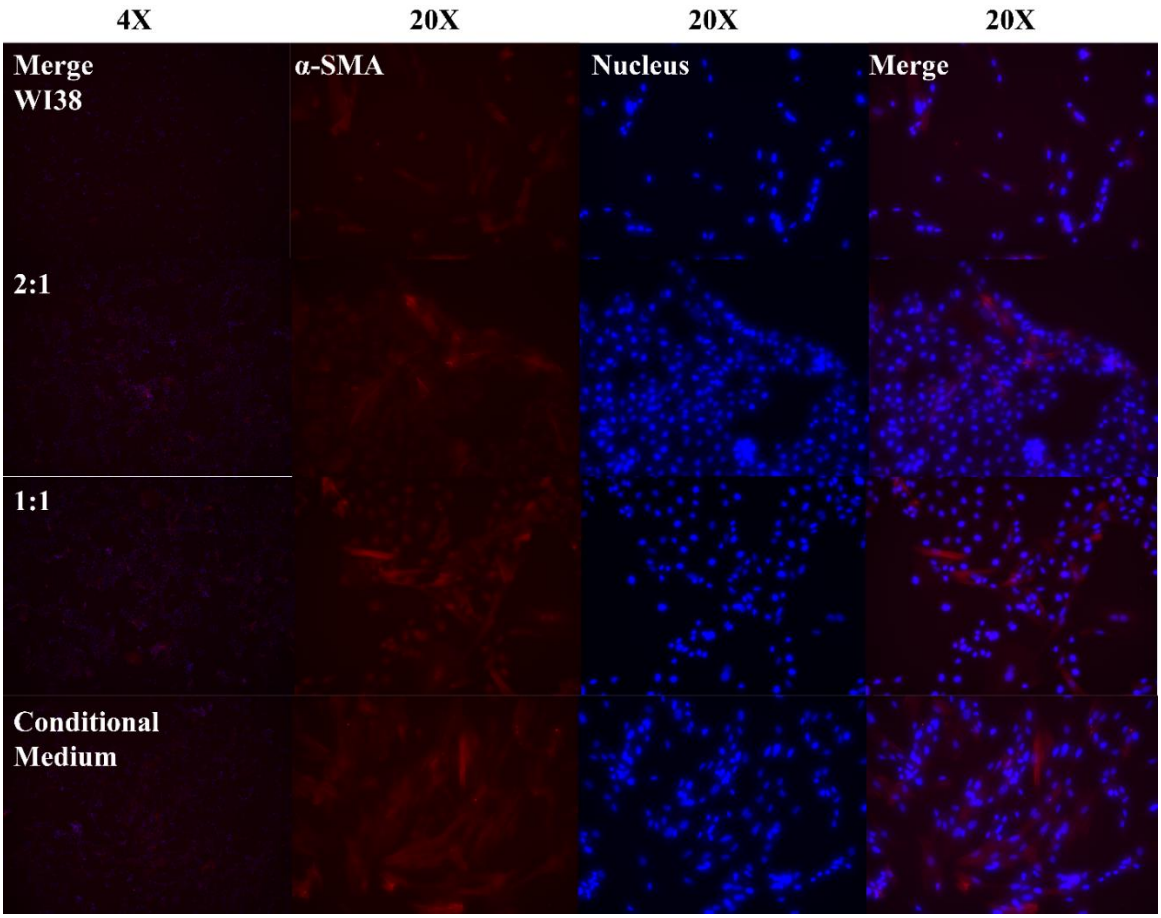

Figure 16: The immunofluorescence assay revealed that A549-iRFP re-educated WI38 cells to CAFs. The α-SMA was imaged in TexasRed channel (λex = 560 nm, λem = 630 nm) with 7 sec exposure time. The nucleus was imaged in DAPI channel (λex = 360 nm, λem = 460 nm) with 1 sec exposure time.

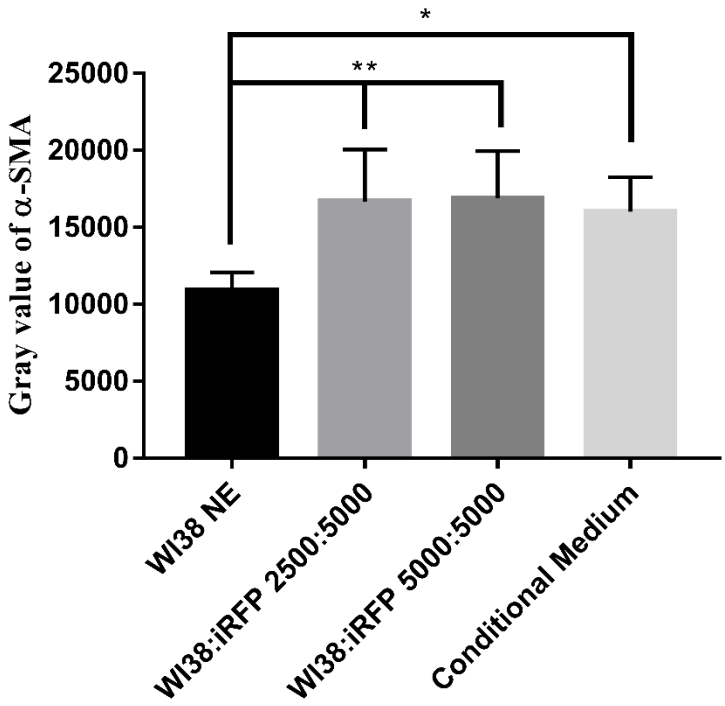

Figure 17: The semi-quantification showed significant increase of α-SMA expression in the co-culture groups and conditional medium group. (* indicates $p<0.05$, ** indicates $p< 0.01$, mean$\pm$SD, N = 6).

4.3.3. Co-culture of A549-iRFP cells with fibroblasts formed MCS with a tight, round shape and rough edges.

A549--iRFP cells were seeded at 4000 cells/well together with 0, 500, 2000, 4000 WI38 cells/well to construct the co-culture MCS. The procedure to build the co-culture MCS was the same as in Chapter 2, except that the co-culture medium is EMEM (10% FBS, 1% pen/strep) instead of DMEM (10% FBS, 1% pen/strep, 1μL/ml puromycin). The morphology of the co-culture MCS and the A549-iRFP MCS showed no significant difference before day 7. At day 7, the co-culture MCS at 1:1 ratio started to show rough edges rather than the smooth edge as seen in A549-iRFP MCS. The rough edges indicated that the cancer cells

were no longer totally tethered by the MCS. This physiological feature was significantly associated with the time the MCS needed to develop metastasis cancer after inoculation in mice. Such rough edges typically were displayed by A549-iRFP MCS after much longer culturing time (>15 days). At day 17, the A549-iRFP MCS in this experiment started to show rough edges but at much less level than the co-culture MCS. These results serve as strong evidence that the WI38 cells had been re-educated to CAFs and were able to promote the cancer cell invasion from MCS (Fig. 18).

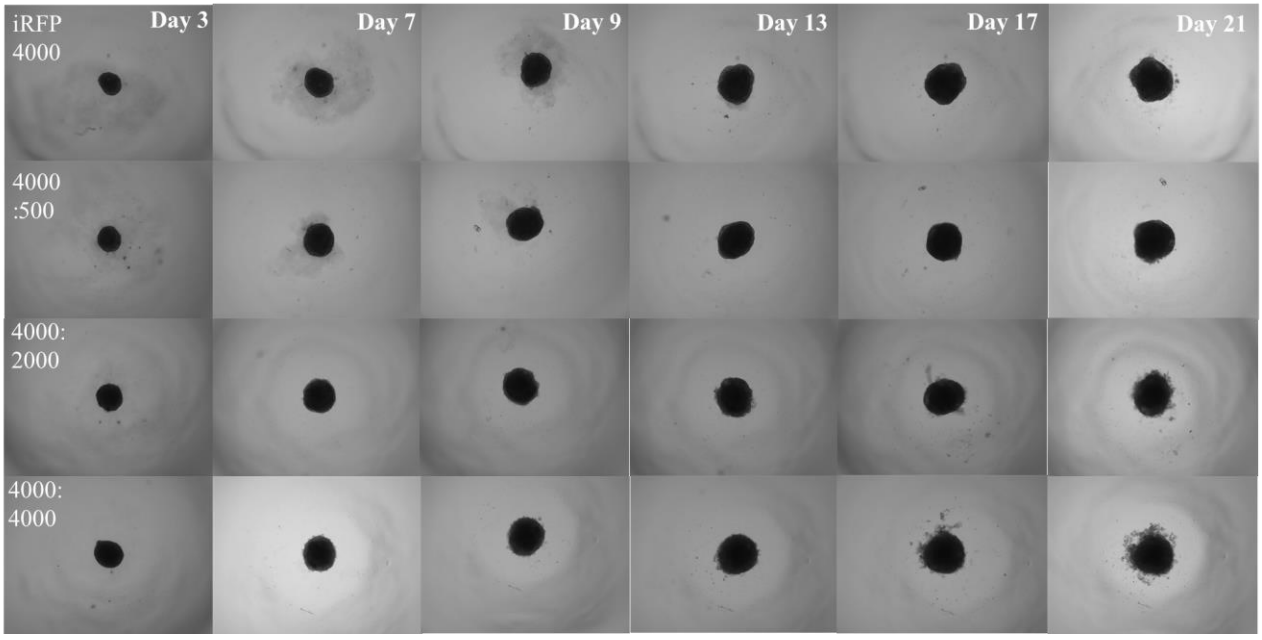

Figure 18: Morphology of A549-iRFP MCS and co-culture MCS. MCS in four groups were monitored every two days under the bright field microscope. Each group has 24 MCS.

4.3.4. Faster growth and higher roughness of Co-culture MCS than MCS of only the A549-iRFP cancer cells. The *in vitro* characterization of co-culture MCS was using the same methods as in Chapter 2. The MCS were scanned every two days on the Odyssey® Infrared Imaging 205 System. The volume was calculated by the ReVisp software using the brightfield images which were taken by a Keyence (US) BZ-X700 fluorescence microscope. The roughness was calculated using the equation Roughness (mm) = $(A_{OL}-A_{IL}) / L_{IL}$, where A_{OL} is the area enclosed by OL, A_{IL} is the area enclosed by IL, and L_{IL} is the length of IL.

The co-cultured MCS had higher fluorescent intensity compared to A549-iRFP alone. However, the fluorescent signal in MCS of only A549-iRFP cells and the co-culture MCS became more similar after the 15 days of culturing, which could be attributed to the relative slow-down of the growth of co-culture MCS compared to MCS with only A549-iRFP cells. This phenomenon could be attributed to the depletion of the WI38 cells in the co-culture MCS. In general fibroblasts have a lower proliferation rate than the cancer cells and the MCS microenvironment limited the fibroblasts' access to nutrients of the culture medium. Alternatively, the slowdown of co-culture MCS growth could also be caused by more severe necrosis in the co-culture MCS.

The initial differences between the volumes of MCS associated with seeding number, where MCS of higher seeding number of cells had a larger volume. However, although the seeding number of co-culture 1:1 group started with two fold as many as seeded cells as MCS of only the A549-iRFP cells alone, the difference in volume on day three after the seeding was less than two fold and not statistically significant. This is probably due to a tighter structure of the co-culture MCS.

The calculated values of roughness showed the same trend as their morphology under the microscope. The unclear, rough edge showed up in the co-culture (1:1) MCS at as early as day 5, when other groups still had smooth surfaces. The co-culture MCS (1:2) displayed remarkable roughness later at day 7. Roughness values of the co-culture MCS (1:1) turned out to be significantly larger than that of the MCS of only A549-iRFP cells. The elevated roughness of MCS may result from the pro-cancer effects of CAFs. Moreover, the higher seeding number of fibroblasts cells lead to higher roughness values, which indicates a positive association between the density of fibroblasts cells in the MCS and the MCS' roughness.

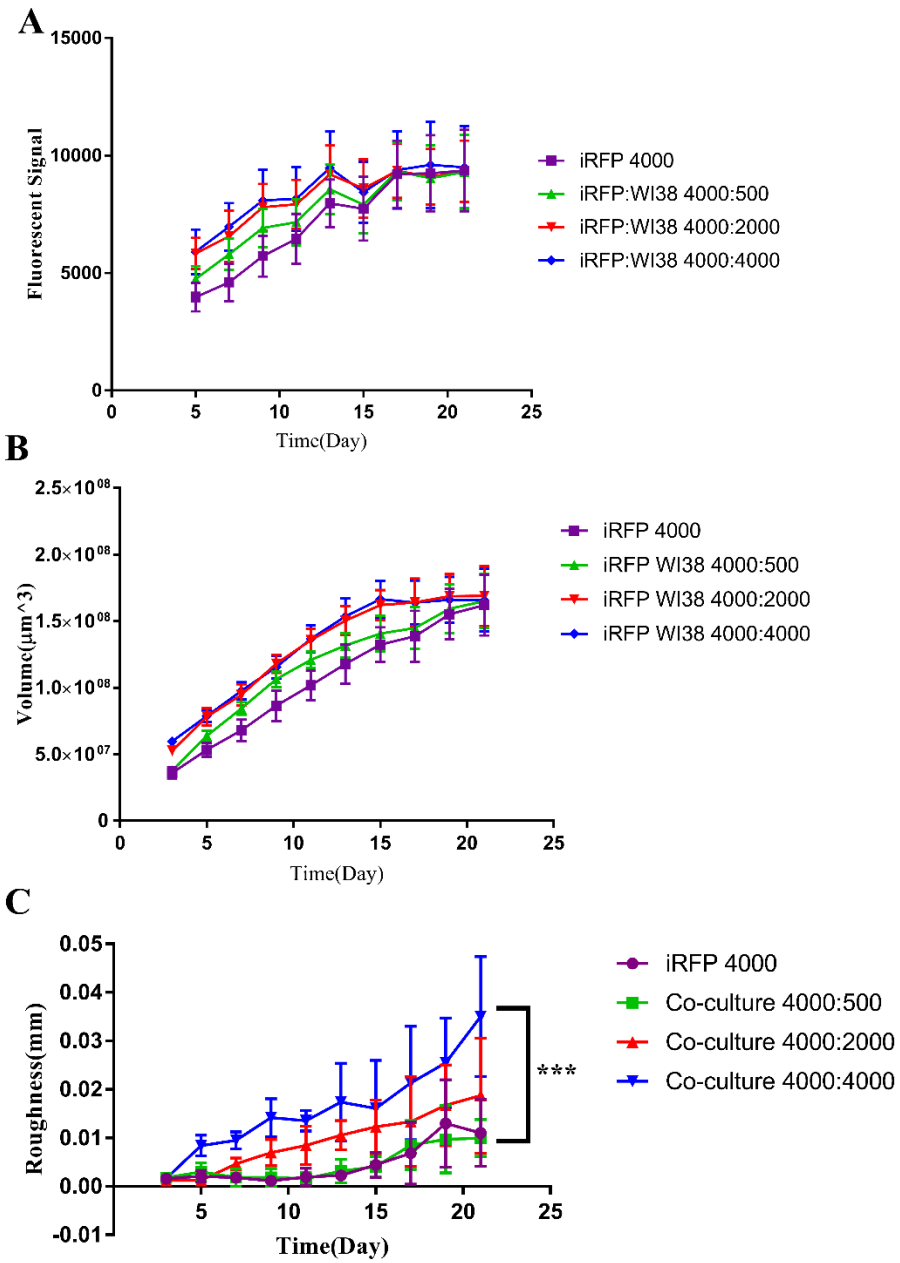

Figure 19: The in vitro characterization of co-culture MCS. The fluorescent signal (A), volume (B) and roughness (C) of MCS increase with time. (Fig. A-B mean±S.D, n=24; Fig. C, *** indicates $p \leq 0.001$, mean±S.D, N = 6)

4.3.5. Immunofluorescence staining of live/dead cells followed by confocal microscopy to characterize the necrotic core of co-culture MCS. To validate that the co-cultured MCS have a necrotic core, both the live and dead cells of the MCS were detected with a immunofluorescence assay. The A549-iRFP cells were co-cultured with WI38 fibroblasts to form MCS at 4000 cells/well density for both A549-iRFP and WI38 cells. The MCS of a diameter around 500 μm were stained at day 5 after seeding. The fluorescent intensity plot for both the green (live cells) and the red (dead cells) channels show the uneven distribution of live and dead cells in the co-culture MCS (Fig. 20). The images showed a necrosis core inside the co-culture MCS, similar to that of MCS of only the A549-iRFP cells.

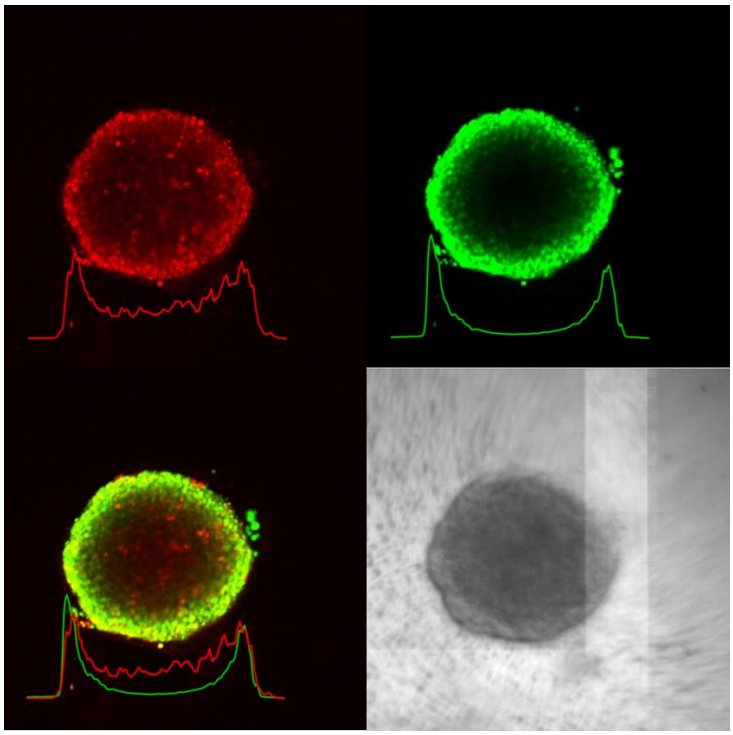

Figure 20: Immunofluorescence imaging of live and dead cells in the co-culture MCS confirmed its necrotic core. Red color indicates dead cells, green color indicates live cells.

4.3.6. Histological studies on co-culture MCS using H&E staining indicates the depletion of fibroblast cells after 6 days of co-culturing. In order to characterize the inner structure of the co-culture MCS, the MCS were constructed by co-culturing A549-iRFP and WI38 cells at the same density of 4000 cells/well. The MCS were grown for 6 days and fixed with 10% formalin, followed by H&E staining as described in Section 2.2.6. However, the inner structure of co-cultured MCS showed no apparent difference with MCS of only A549-iRFP cells. Both co-culture and MCS of only cancer cells showed a loose internal structure, which is consistent with the presence of a necrotic core after 6 days of culture (Fig. 22). Co-cultured MCS 3 days after the seeding were also fixed and stained with H&E (Fig. 21). As the MCS needed to be visualized during the embedding process in the histology study, A549-iRFP and WI38 cells were both seeded at higher density of 10000 cells/well to construct such MCS of shorter growth time. MCS of only A549-iRFP cells at 20000 cells/well seeding density was characterized as a control for comparison. Without being co-cultured with fibroblast cells, the MCS showed a loose inner structure, which is similar to previous results. In contrast, the co-cultured MCS showed a dense internal structure in the center. The yellow arrows point out cells of spindle-like morphology, which are fibroblast cells. The fibroblast cells were aggregated at the center of the MCS and showed a skeleton-like structure. The slower proliferation of fibroblast cells would explain why WI38 cells were only present at the core of MCS. Taken together, these results confirm the initial presence of the fibroblast WI38 cells in the co-culture MCS, followed by their depletion after being cultured for 3-6 days, which, as mentioned before,

would explain the slowdown in the increase of fluorescence and the volume of the co-culture MCS.

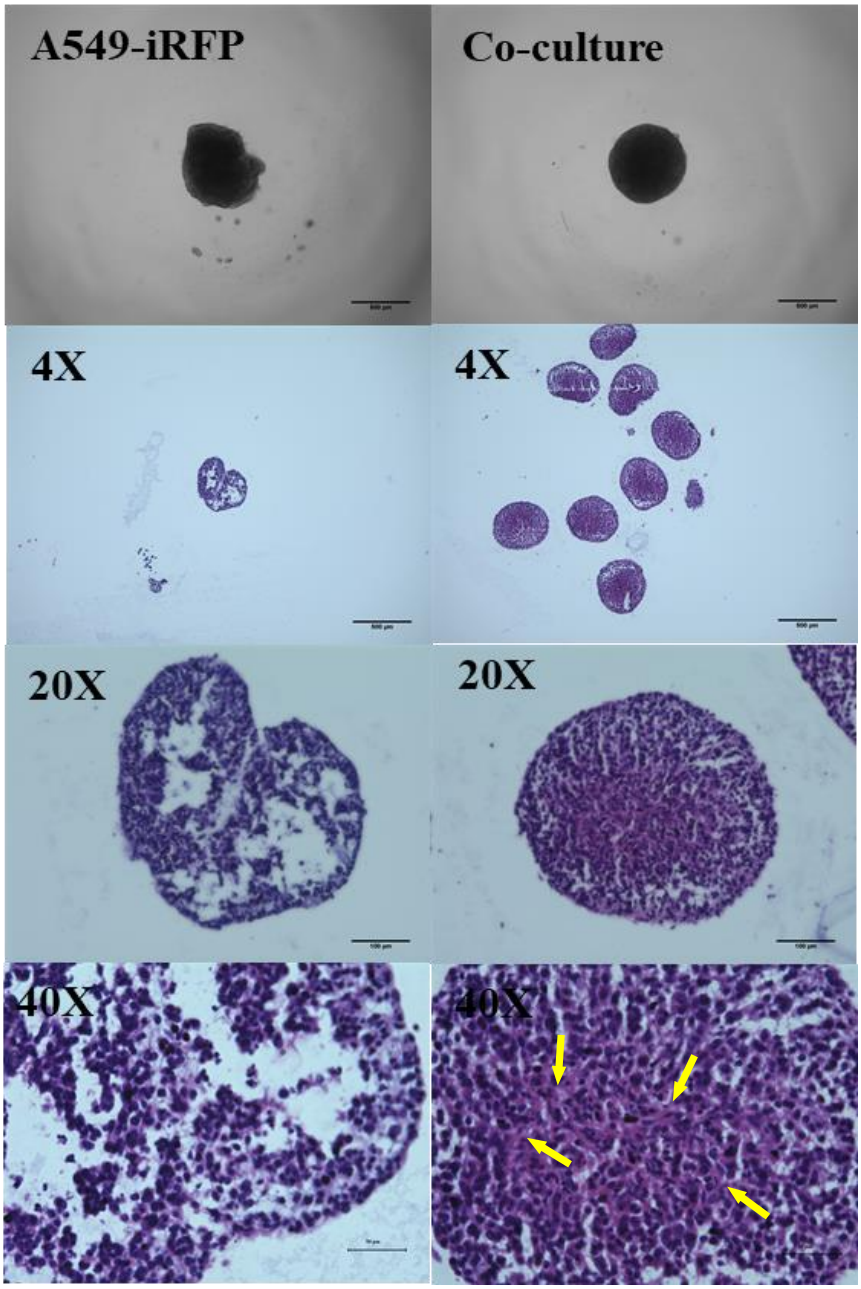

Figure 21: Histological Imaging (H&E staining) of co-culture and single culture MCS after being cultured for 3 days.

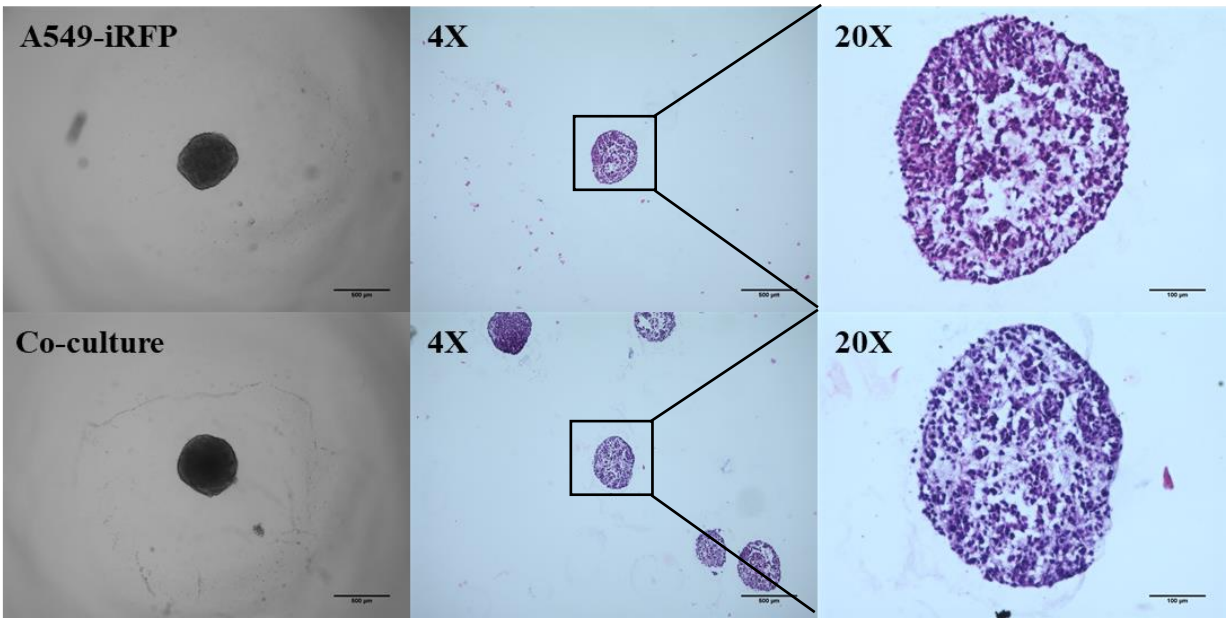

Figure 22: Histological Imaging (H&E staining) of co-culture and single culture MCS after being cultured for 6 days.

4.3.7. Attempted Identification of CAFs in co-culture MCS by Immunohistochemistry (IHC).

To confirm the existence of CAFs in the co-cultured MCS, an immunohistochemistry assay was performed day 3 after seeding on both the co-culture MCS and MCS of only cancer cells. MCS were constructed as described in Section 4.2.4. The immunofluorescence staining on paraffin-embedded samples was optimized with overnight incubation of the primary-antibody. However, in both co-culture MCS and MCS of only the A549-iRFP cells, there was no positive fluorescent signal at 568 nm that would represent the a-SMA (Fig. 23). This result contradicted with the H&E staining of co-culture MCS, which

clearly showed fibroblast-like cells in the center of MCS. One possible reason for this observation is that during the paraffin-embedding process, the binding sites for the antibody have been blocked, which is a common problem of IHC assay on the paraffin-embedded samples.

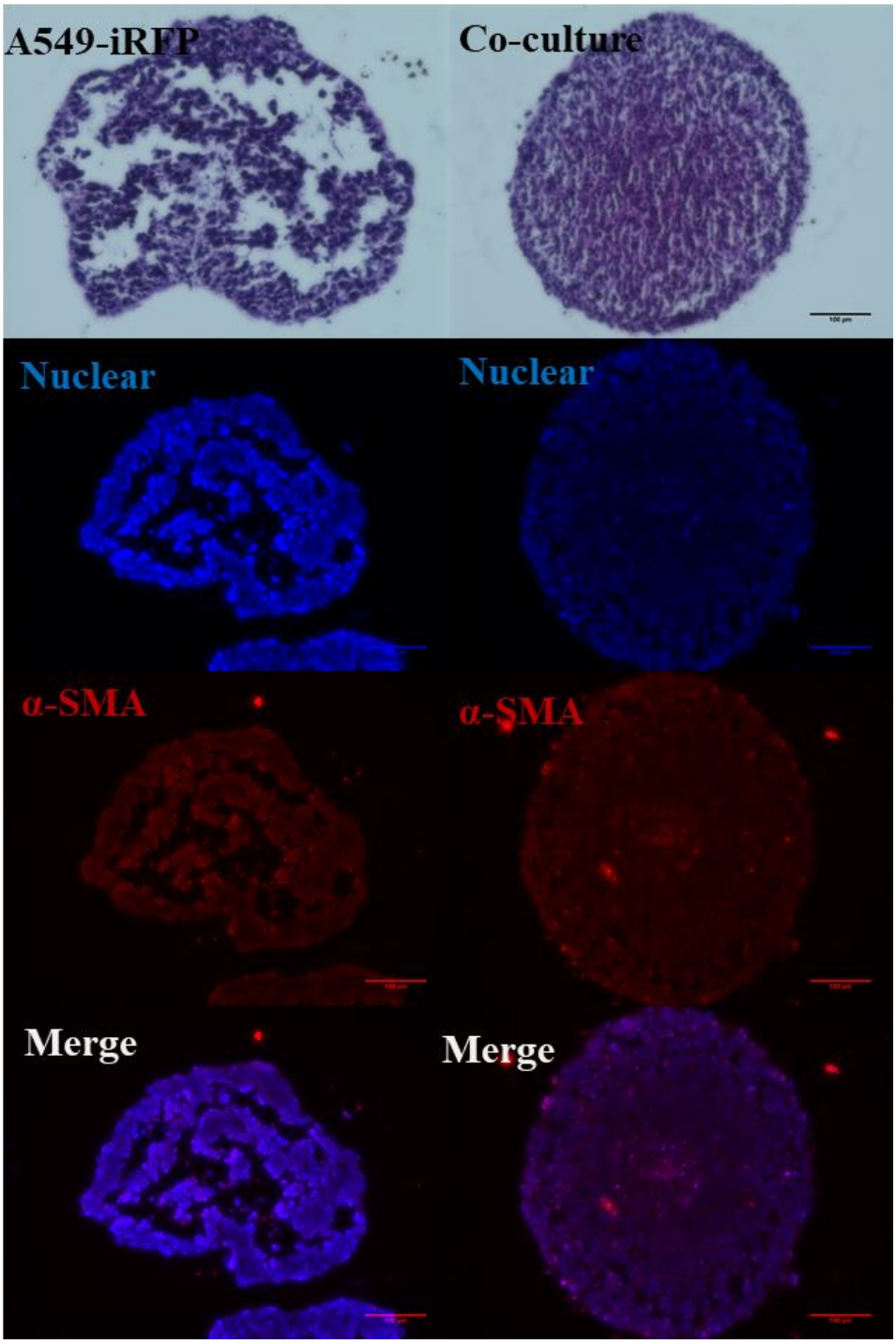

Figure 23: Immunohistochemistry (IHC) assay on MCS to identify the existence of CAFs.

4.4 Discussion

In this chapter, we first identified the pro-proliferation effect and positive results of the biomarker study which indicated a transformation of normal fibroblasts to cancer-associated fibroblasts (CAFs) in monolayer cells. Then, we constructed a co-cultured MCS that consisted of A549-iRFP lung cancer cells and WI38 normal human fibroblast cells. The 3D MCS showed higher fluorescent intensity in the co-culture group than the group of only the A549-iRFP cancer cells, indicating that CAFs promoted tumor growth.

The morphology of the co-cultured MCS features a round shape, a tight structure, and quicker development of roughness. Co-culturing the A549-iRFP cells and WI38 cells at the same seeding density started to show the rough edges on the 5th day after seeding, which is much earlier than the time for MCS of only the A549-iRFP cells. The inner structure of co-cultured MCS was illustrated by histological studies using the H&E staining. Interestingly, there were no clear, spindle-like cells in the co-cultured MCS after 6 days of growth. The depletion of fibroblasts cells was speculated, which lead me to study the structure of the co-cultured MCS at an earlier time. Thus the co-culture MCS that were grown for only 3 days were fixed, and stained with H&E. At this earlier time point, a much denser structure and the fibroblasts-like cells were observed at the center of the co-culture MCS, compared to MCS of only the A549-iRFP cells. However, there was no positive staining in the immunohistochemistry assay that would have detected the presence of CAFs in the co-cultured MCS. One possible reason for this discrepancy is that the paraffin embedding blocked the binding sites of α-SMA to give a false negative result. Overall, the co-cultured fibroblasts inside the MCS under our studies were shown to promote the cancer proliferation and invasion.

The fluorescent signal of A549-iRFP cells reflected the tumor promoting effect of CAFs. In the monolayer studies, the co-culture group showed significantly larger fluorescent signal compared monolayers of only A549-iRFP cells. The WI38 cells alone as a control did not have a fluorescent signal in the 700 nm wavelength. In 3D MCS, the co-cultured MCS showed higher fluorescent signal and larger volume than MCS of A549-iRFP alone over the first 15 days of MCS culturing. The higher fluorescent signal of the co-cultured MCS at day 5 also specifically indicated a tumor-promoting effect of CAFs in the early days. After 15 days, the fluorescent signal of all the MCS groups trended toward the same level, which can be explained either by the depletion of fibroblasts or by a more severe necrosis in the core of MCS. Overall, the co-culture studies illustrated a pro-tumor effect of CAFs both in monolayer and in MCS.

An immunofluorescence assay was used to detect α-SMA, which is the biomarker of CAFs. In the monolayer study, 6 cells randomly selected to semi-quantify the presence of α-SMA in co-culture, share medium and WI38 alone groups. The significantly higher grey value of α-SMA in the co-culture and the shared medium groups confirmed the existence of CAFs. These results indicate that the re-education of normal fibroblasts to CAFs took place both in direct and indirect co-cultures. The results of our study are consistent with a previous study where WI38 and A549 cells were grown separately but shared medium in a fluid set up [10]. However, in the MCS study, no α-SMA signal was detected in the co-cultured MCS by the immunohistochemistry. This is probably due to the potential blocking of the anti-body binding sites by the paraffin. An additional target retrieval procedure may help overcome the blocking effect [83].

The most important finding of our co-cultured MCS study is the earlier formation of the rough edge in the co-culture MCS compared to MCS of A549-iRFP cells only. In Chapter 3, the

roughness of the inoculated MCS was shown to correlate negatively with the time needed to develop metastatic cancer ($p=0.0299$) in the MCS inoculated mice. Therefore, the co-culture MCS with a relatively small volume but a large roughness value can be inoculated into mice with a smaller needle. This potential optimization would further reduce the surgical trauma caused by MCS inoculation into the lung parenchyma. Further, the large roughness value of the co-culture MCS in this study indicated that they maintained a high invasive capacity over 20 days of culturing, which in turn suggest that such co-cultured MCS, upon inoculation into mice, would manifest four-stage cancer progression that is similar to what is reported in Chapter 2.

Chapter 5: Summary

Lung cancer xenograft serves as one of the most useful tools in evaluating therapeutic efficacy and understanding lung cancer biology. Subcutaneous xenografts are typically the predominant model in screening drug candidates of chemotherapy, but its use is associated with the unfaithful prediction due to the lack of reflection of cancer metastasis [25, 39]. The utilization of orthotopic lung cancer model has resulted in an improved reflection of the tumor microenvironment, such as hypoxia. However, the current method of constructing orthotopic lung cancer xenograft features premature leakage of the cancer cells to both sides of the lung within five days, which generates a quick artifact of metastasis and thus belies the development and progression of lung cancer as seen in the clinic [43, 45, 47, 48]. In order to better optimize this model, a novel implantation method based on intrapulmonary inoculation of multicellular spheroids (MCS) is developed and present in this thesis.

A549-iRFP MCS have been constructed and its volume, viability, morphology and fluorescent signal have been characterized. Compared to suspended cells, the MCS better mimic the condensed morphology of primary solid tumors that present a barrier for drug penetration. The A549-iRFP MCS showed strong correlation with the volume and viability of MCS, which indicates the potential of using the fluorescent signal to reflect the cancer growth. Since the bright and stable signal from near-infrared fluorescent protein that expressed in A549-iRFP cells has low absorbance and less light scattering, which allows the non-invasive in vivo imaging. Therefore, the fluorescent signal of A549-iRFP MCS can be utilized to reflect the cancer growth.

The inoculation procedure is similar to the time needed to inject suspended cells to build tumor xenografts in mice. Each MCS inoculation took about 20 minutes, allowing one experienced researcher to inoculate 20 mice per day. Since the location of primary lung adenocarcinoma is typically in the periphery of lung parenchyma, the inoculation of A549-iRFP MCS mimics the initiation location of the primary solid adenocarcinoma. For squamous cell carcinoma, which generally grows in the center of the lung, tracheal intubation could help in delivering MCS into the lung [5].

In this study, the association between the MCS roughness and the time needed for metastasis suggests that the more invasive morphology of MCS can lead to an early intrathoracic metastasis of orthotopic lung cancer model. The equation of calculating these rough edges is derived from the equation of quantifying invasiveness [65, 84]. The value of roughness indicates the average length of these rough edges. The higher length of roughness represents the farther distance of cancer cells invasive into the surrounding medium. By associating with the in vivo results that mice inoculated MCS with larger roughness value showed fluorescent signals on both sides of the lung earlier than mice inoculated with MCS with less roughness. From both in vitro morphology changes and in vivo early metastasis, these rough edges could reflect a more aggressive cancer growth. A series of biological studies will be done to demonstrate the MCS with rough edges exhibit greater cell growth potential than MCS without rough edges.

Organoid implantation has been reported in constructing a colorectal cancer model in many literatures [85]. GEMM have featured with the reliable prediction of targeting therapy and faithful recapitulation of genetic variations. However, the anatomical location of the primary tumor in GEMM of colon cancer is incorrect. This is because traditional GEMMs harboring germline Apc mutations frequently develop small intestinal, rather than colonic lesions. By

engrafted genetically engineered organoid into the mucosal layer of the mouse colon, a novel orthotopic colon cancer model was developed. The *ex vivo* modification of human organoid provides a flexible, fast, and low-cost platform to study colorectal cancer development. By accurately transplanted the genetically modified organoids into the mucosal layer of mouse colon, it avoids the incorrect location that tumor initiate [86]. The combination of genetic tools and surgical approaches could further facilitate the development of the mouse model. In our study, we first developed the method to inoculate sphere-like cancer cell aggregate into the mice lung. This approach is also easily adapted for the orthotopic engraftment of lung cancer organoids for the production of histopathologically accurate pre-clinical human cancer models.

In summary, a novel lung cancer model was constructed based on orthotopic inoculation of MCS of fluorescently labeled human lung cancer cells. The surgical procedure for the model achieved high postoperative survival rate and allowed cancer development that mimicked four clinical stages of NSCLC. Collectively this new animal model will help drive the development of small molecules for against the metastatic non-small cell lung cancer.

References

1. Siegel, R.L., K.D. Miller, and A. Jemal, *Cancer statistics, 2019.* CA Cancer J Clin, 2019. **69**(1): p. 7-34.
2. Zappa, C. and S.A. Mousa, *Non-small cell lung cancer: current treatment and future advances.* Transl Lung Cancer Res, 2016. **5**(3): p. 288-300.
3. Furrukh, M., *Tobacco Smoking and Lung Cancer: Perception-changing facts.* Sultan Qaboos Univ Med J, 2013. **13**(3): p. 345-58.
4. Gazdar, A.F., P.A. Bunn, and J.D. Minna, *Small-cell lung cancer: what we know, what we need to know and the path forward (vol 17, pg 725, 2017).* Nature Reviews Cancer, 2017. **17**(12): p. 765-765.
5. Lemjabbar-Alaoui, H., et al., *Lung cancer: Biology and treatment options.* Biochim Biophys Acta, 2015. **1856**(2): p. 189-210.
6. Travis, W.D., et al., *The 2015 World Health Organization Classification of Lung Tumors: Impact of Genetic, Clinical and Radiologic Advances Since the 2004 Classification.* J Thorac Oncol, 2015. **10**(9): p. 1243-1260.
7. Reck, M. and K.F. Rabe, *Precision Diagnosis and Treatment for Advanced Non-Small-Cell Lung Cancer.* N Engl J Med, 2017. **377**(9): p. 849-861.
8. Altorki, N.K., et al., *The lung microenvironment: an important regulator of tumour growth and metastasis.* Nat Rev Cancer, 2019. **19**(1): p. 9-31.
9. Han, X., et al., *Transdifferentiation of lung adenocarcinoma in mice with Lkb1 deficiency to squamous cell carcinoma.* Nat Commun, 2014. **5**: p. 3261.

10. Yu, T., et al., *Cancer-associated fibroblasts promote non-small cell lung cancer cell invasion by upregulation of glucose-regulated protein 78 (GRP78) expression in an integrated bionic microfluidic device.* Oncotarget, 2016. **7**(18): p. 25593-603.

11. Wang, L., et al., *Cancer-associated fibroblasts enhance metastatic potential of lung cancer cells through IL-6/STAT3 signaling pathway.* Oncotarget, 2017. **8**(44): p. 76116-76128.

12. Ito, M., et al., *Prognostic impact of cancer-associated stromal cells in patients with stage I lung adenocarcinoma.* Chest, 2012. **142**(1): p. 151-158.

13. DeVita, V.T., Jr. and E. Chu, *A history of cancer chemotherapy.* Cancer Res, 2008. **68**(21): p. 8643-53.

14. Fidler, I.J. and I.R. Hart, *Biological diversity in metastatic neoplasms: origins and implications.* Science, 1982. **217**(4564): p. 998-1003.

15. Day, C.P., G. Merlino, and T. Van Dyke, *Preclinical mouse cancer models: a maze of opportunities and challenges.* Cell, 2015. **163**(1): p. 39-53.

16. Talmadge, J.E., et al., *Murine models to evaluate novel and conventional therapeutic strategies for cancer.* Am J Pathol, 2007. **170**(3): p. 793-804.

17. Peterson, J.K. and P.J. Houghton, *Integrating pharmacology and in vivo cancer models in preclinical and clinical drug development.* Eur J Cancer, 2004. **40**(6): p. 837-44.

18. Bibby, M.C., *Orthotopic models of cancer for preclinical drug evaluation: advantages and disadvantages.* European Journal of Cancer, 2004. **40**(6): p. 852-857.

19. Cowen, S.E., M.C. Bibby, and J.A. Double, *Characterization of the Vasculature within a Murine Adenocarcinoma Growing in Different Sites to Evaluate the Potential of Vascular Therapies.* Acta Oncologica, 1995. **34**(3): p. 357-360.

20. Kocaturk, B. and H.H. Versteeg, *Orthotopic injection of breast cancer cells into the mammary fat pad of mice to study tumor growth.* J Vis Exp, 2015(96).

21. Ricard, C., et al., *An orthotopic glioblastoma mouse model maintaining brain parenchymal physical constraints and suitable for intravital two-photon microscopy.* J Vis Exp, 2014(86).

22. Kagadis, G.C., et al., *In vivo small animal imaging: current status and future prospects.* Med Phys, 2010. **37**(12): p. 6421-42.

23. Teicher, B.A., *Tumor models for efficacy determination.* Mol Cancer Ther, 2006. **5**(10): p. 2435-43.

24. Hidalgo, M., et al., *Patient-derived xenograft models: an emerging platform for translational cancer research.* Cancer Discov, 2014. **4**(9): p. 998-1013.

25. Gengenbacher, N., M. Singhal, and H.G. Augustin, *Preclinical mouse solid tumour models: status quo, challenges and perspectives.* Nat Rev Cancer, 2017. **17**(12): p. 751-765.

26. Ben-David, U., R. Beroukhim, and T.R. Golub, *Genomic evolution of cancer models: perils and opportunities.* Nat Rev Cancer, 2019. **19**(2): p. 97-109.

27. Gao, H., et al., *High-throughput screening using patient-derived tumor xenografts to predict clinical trial drug response.* Nature Medicine, 2015. **21**(11): p. 1318-1325.

28. Aparicio, S., M. Hidalgo, and A.L. Kung, *Examining the utility of patient-derived xenograft mouse models.* Nat Rev Cancer, 2015. **15**(5): p. 311-6.

29. Kemp, C.J., *Animal Models of Chemical Carcinogenesis: Driving Breakthroughs in Cancer Research for 100 Years.* Cold Spring Harb Protoc, 2015. **2015**(10): p. 865-74.

30. Abel, E.L., et al., *Multi-stage chemical carcinogenesis in mouse skin: fundamentals and applications.* Nat Protoc, 2009. **4**(9): p. 1350-62.

31. Westcott, P.M., et al., *The mutational landscapes of genetic and chemical models of Kras-driven lung cancer.* Nature, 2015. **517**(7535): p. 489-92.

32. Gurley, K.E., R.D. Moser, and C.J. Kemp, *Induction of Liver Tumors in Mice with N-Ethyl-N-Nitrosourea or N-Nitrosodiethylamine.* Cold Spring Harb Protoc, 2015. **2015**(10): p. 941-2.

33. Gurley, K.E., R.D. Moser, and C.J. Kemp, *Induction of Colon Cancer in Mice with 1,2-Dimethylhydrazine.* Cold Spring Harb Protoc, 2015. **2015**(9): p. pdb prot077453.

34. Finlay, C.A., *p53 loss of function: implications for the processes of immortalization and tumorigenesis.* Bioessays, 1992. **14**(8): p. 557-60.

35. Kersten, K., et al., *Genetically engineered mouse models in oncology research and cancer medicine.* EMBO Mol Med, 2017. **9**(2): p. 137-153.

36. DuPage, M., A.L. Dooley, and T. Jacks, *Conditional mouse lung cancer models using adenoviral or lentiviral delivery of Cre recombinase.* Nature Protocols, 2009. **4**(7): p. 1064-1072.

37. Schonhuber, N., et al., *A next-generation dual-recombinase system for time- and host-specific targeting of pancreatic cancer.* Nat Med, 2014. **20**(11): p. 1340-1347.

38. Singh, M., et al., *Assessing therapeutic responses in Kras mutant cancers using genetically engineered mouse models.* Nature Biotechnology, 2010. **28**(6): p. 585-U74.

39. Francia, G., et al., *Mouse models of advanced spontaneous metastasis for experimental therapeutics.* Nat Rev Cancer, 2011. **11**(2): p. 135-41.

40. Killion, J.J., R. Radinsky, and I.J. Fidler, *Orthotopic models are necessary to predict therapy of transplantable tumors in mice.* Cancer Metastasis Rev, 1998. **17**(3): p. 279-84.

41. Niu, P.G., et al., *Cardamonin Inhibits Metastasis of Lewis Lung Carcinoma Cells by Decreasing mTOR Activity.* PLoS One, 2015. **10**(5): p. e0127778.

42. Graves, E.E., et al., *Hypoxia in models of lung cancer: implications for targeted therapeutics.* Clin Cancer Res, 2010. **16**(19): p. 4843-52.

43. Mordant, P., et al., *Bioluminescent orthotopic mouse models of human localized non-small cell lung cancer: feasibility and identification of circulating tumour cells.* PLoS One, 2011. **6**(10): p. e26073.

44. Kraus-Berthier, L., et al., *Histology and sensitivity to anticancer drugs of two human non-small cell lung carcinomas implanted in the pleural cavity of nude mice.* Clin Cancer Res, 2000. **6**(1): p. 297-304.

45. Madero-Visbal, R.A., et al., *Bioluminescence imaging correlates with tumor progression in an orthotopic mouse model of lung cancer.* Surgical Oncology-Oxford, 2012. **21**(1): p. 23-29.

46. Justilien, V. and A.P. Fields, *Utility and applications of orthotopic models of human non-small cell lung cancer (NSCLC) for the evaluation of novel and emerging cancer therapeutics.* Curr Protoc Pharmacol, 2013. **62**: p. Unit 14 27.

47. Peng, L., et al., *Development of a novel orthotopic non-small cell lung cancer model and therapeutic benefit of 2 '-(2-bromohexadecanoyl)-docetaxel conjugate nanoparticles.* Nanomedicine-Nanotechnology Biology and Medicine, 2014. **10**(7): p. 1497-1506.

48. Lai, C.W., et al., *Using Dual Fluorescence Reporting Genes to Establish an In Vivo Imaging Model of Orthotopic Lung Adenocarcinoma in Mice.* Molecular Imaging and Biology, 2016. **18**(6): p. 849-859.

49. Weiss, I.D., et al., *In the hunt for therapeutic targets: mimicking the growth, metastasis, and stromal associations of early-stage lung cancer using a novel orthotopic animal model.* J Thorac Oncol, 2015. **10**(1): p. 46-58.

50. Nakano, T., et al., *Establishment of highly metastatic KRAS mutant lung cancer cell sublines in long-term three-dimensional low attachment cultures.* PLoS One, 2017. **12**(8): p. e0181342.

51. Saxena, M. and G. Christofori, *Rebuilding cancer metastasis in the mouse.* Mol Oncol, 2013. **7**(2): p. 283-96.

52. Yao, R., R. Lecomte, and E.S. Crawford, *Small-animal PET: what is it, and why do we need it?* J Nucl Med Technol, 2012. **40**(3): p. 157-65.

53. Hoffman, R.M., *Application of GFP imaging in cancer.* Lab Invest, 2015. **95**(4): p. 432-52.

54. Rice, W.L., et al., *In vivo tomographic imaging of deep-seated cancer using fluorescence lifetime contrast.* Cancer Res, 2015. **75**(7): p. 1236-43.

55. Weissleder, R., *A clearer vision for in vivo imaging.* Nat Biotechnol, 2001. **19**(4): p. 316-7.

56. Filonov, G.S., et al., *Bright and stable near-infrared fluorescent protein for in vivo imaging.* Nature Biotechnology, 2011. **29**(8): p. 757-U133.

57. Zanoni, M., et al., *3D tumor spheroid models for in vitro therapeutic screening: a systematic approach to enhance the biological relevance of data obtained*. Scientific Reports, 2016. **6**.

58. Mehta, G., et al., *Opportunities and challenges for use of tumor spheroids as models to test drug delivery and efficacy*. Journal of Controlled Release, 2012. **164**(2): p. 192-204.

59. Valta, M.P., et al., *Spheroid culture of LuCaP 136 patient-derived xenograft enables versatile preclinical models of prostate cancer*. Clin Exp Metastasis, 2016. **33**(4): p. 325-37.

60. Sethi, P., et al., *3D tumor tissue analogs and their orthotopic implants for understanding tumor-targeting of microenvironment-responsive nanosized chemotherapy and radiation.* Nanomedicine-Nanotechnology Biology and Medicine, 2015. **11**(8): p. 2013-2023.

61. Edmondson, R., et al., *Three-Dimensional Cell Culture Systems and Their Applications in Drug Discovery and Cell-Based Biosensors.* Assay and Drug Development Technologies, 2014. **12**(4): p. 207-218.

62. Langhans, S.A., *Three-Dimensional in Vitro Cell Culture Models in Drug Discovery and Drug Repositioning.* Front Pharmacol, 2018. **9**: p. 6.

63. Sutherland, R.M., J.A. McCredie, and W.R. Inch, *Growth of multicell spheroids in tissue culture as a model of nodular carcinomas.* J Natl Cancer Inst, 1971. **46**(1): p. 113-20.

64. Lohr, M., et al., *Implanting Glioblastoma Spheroids into Rat Brains and Monitoring Tumor Growth by MRI Volumetry*. Methods Mol Biol, 2017. **1622**: p. 149-159.

65. Carey, S.P., et al., *Leading malignant cells initiate collective epithelial cell invasion in a three-dimensional heterotypic tumor spheroid model.* Clin Exp Metastasis, 2013. **30**(5): p. 615-30.

66. Bredholt, G., et al., *Tumor necrosis is an important hallmark of aggressive endometrial cancer and associates with hypoxia, angiogenesis and inflammation responses.* Oncotarget, 2015. **6**(37): p. 39676-39691.

67. Su, Z., et al., *Apoptosis, autophagy, necroptosis, and cancer metastasis.* Mol Cancer, 2015. **14**: p. 48.

68. Carver, B.S. and P.P. Pandolfi, *Mouse modeling in oncologic preclinical and translational research.* Clin Cancer Res, 2006. **12**(18): p. 5305-11.

69. Lampreht Tratar, U., S. Horvat, and M. Cemazar, *Transgenic Mouse Models in Cancer Research.* Front Oncol, 2018. **8**: p. 268.

70. Zhang, Z., T. Hatori, and H. Nonaka, *An experimental model of brain metastasis of lung carcinoma.* Neuropathology, 2008. **28**(1): p. 24-28.

71. Vikis, H.G., A.L. Rymaszewski, and J.W. Tichelaar, *Mouse models of chemically-induced lung carcinogenesis.* Front Biosci (Elite Ed), 2013. **5**: p. 939-46.

72. Westcott, P.M.K., et al., *The mutational landscapes of genetic and chemical models of Kras-driven lung cancer.* Nature, 2015. **517**(7535): p. 489-+.

73. Schaffer, B.E., et al., *Loss of p130 accelerates tumor development in a mouse model for human small-cell lung carcinoma.* Cancer Res, 2010. **70**(10): p. 3877-83.

74. Herbst, R.S., D. Morgensztern, and C. Boshoff, *The biology and management of non-small cell lung cancer.* Nature, 2018. **553**(7689): p. 446-454.

75. Ohlund, D., et al., *Distinct populations of inflammatory fibroblasts and myofibroblasts in pancreatic cancer.* Journal of Experimental Medicine, 2017. **214**(3): p. 579-596.

76. Chen, X.M. and E.W. Song, *Turning foes to friends: targeting cancer-associated fibroblasts.* Nature Reviews Drug Discovery, 2019. **18**(2): p. 99-115.

77. Gaggioli, C., et al., *Fibroblast-led collective invasion of carcinoma cells with differing roles for RhoGTPases in leading and following cells.* Nat Cell Biol, 2007. **9**(12): p. 1392-400.

78. Kuperwasser, C., et al., *Reconstruction of functionally normal and malignant human breast tissues in mice.* Proc Natl Acad Sci U S A, 2004. **101**(14): p. 4966-71.

79. Orimo, A., et al., *Stromal fibroblasts present in invasive human breast carcinomas promote tumor growth and angiogenesis through elevated SDF-1/CXCL12 secretion.* Cell, 2005. **121**(3): p. 335-348.

80. Zhang, X.H., et al., *Selection of bone metastasis seeds by mesenchymal signals in the primary tumor stroma.* Cell, 2013. **154**(5): p. 1060-1073.

81. Grum-Schwensen, B., et al., *Suppression of tumor development and metastasis formation in mice lacking the S100A4(mts1) gene.* Cancer Res, 2005. **65**(9): p. 3772-80.

82. Amann, A., et al., *Development of an innovative 3D cell culture system to study tumour--stroma interactions in non-small cell lung cancer cells.* PLoS One, 2014. **9**(3): p. e92511.

83. Shi, S.R., Y. Shi, and C.R. Taylor, *Antigen retrieval immunohistochemistry: review and future prospects in research and diagnosis over two decades.* J Histochem Cytochem, 2011. **59**(1): p. 13-32.

84. Szade, K., et al., *Spheroid-plug model as a tool to study tumor development, angiogenesis, and heterogeneity in vivo (vol 37, pg 2481, 2016).* Tumor Biology, 2016. **37**(9): p. 12901-12901.

85. Li, M. and J.C. Izpisua Belmonte, *Organoids - Preclinical Models of Human Disease.* N Engl J Med, 2019. **380**(6): p. 569-579.

86. O'Rourke, K.P., et al., *Transplantation of engineered organoids enables rapid generation of metastatic mouse models of colorectal cancer*. Nature Biotechnology, 2017. **35**(6): p. 577-+.